JCTC Journal of Chemical Theory and Computation

pubs.acs.org/JCTC Article

Mapping Quantum Chemical Dynamics Problems to Spin-Lattice Simulators

Debadrita Saha, Srinivasan S. Iyengar,* Philip Richerme,* Jeremy M. Smith, and Amr Sabry

Cite This: *J. Chem. Theory Comput.* 2021, 17, 6713−6732 Read Online

ACCESS | Metrics & More | Article Recommendations

ABSTRACT: The accurate computational determination of chemical, materials, biological, and atmospheric properties has a critical impact on a wide range of health and environmental problems, but is deeply limited by the computational scaling of quantum mechanical methods. The complexity of quantum chemical studies arises from the steep algebraic scaling of electron correlation methods and the exponential scaling in studying nuclear dynamics and molecular flexibility. To date, efforts to apply quantum hardware to such quantum chemistry problems have focused primarily on electron correlation. Here, we provide a framework that allows for the solution of quantum chemical nuclear dynamics by mapping these to quantum spin-lattice simulators. Using the example case of a short-strong hydrogen-bonded system, we construct the Hamiltonian for the nuclear degrees of freedom on a single Born−Oppenheimer surface and show how it can be transformed to a generalized Ising model Hamiltonian. We then demonstrate a method to determine the local fields and spin−spin couplings needed to identically match the molecular and spin-lattice Hamiltonians. We describe a protocol to determine the on-site and intersite coupling parameters of this Ising Hamiltonian from the Born−Oppenheimer potential and nuclear kinetic energy operator. Our approach represents a paradigm shift in the methods used to study quantum nuclear dynamics, opening the possibility to solve both electronic structure and nuclear dynamics problems using quantum computing systems.

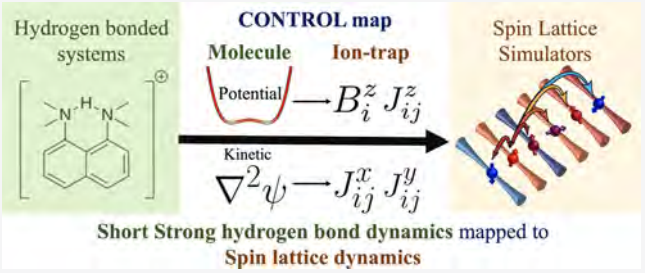

I. INTRODUCTION

The quantum mechanical treatment of electrons and nuclei is critical for a wide range of problems that are of significance to biological, materials, and atmospheric studies. For example, hydrogen transfer processes are ubiquitous in reactions critical to human health, alternative energy sources, food security, and environmental remediation.[1] Yet, the detailed treatment of such problems is confounded by the presence of nontrivial quantum nuclear effects, such as hydrogen tunneling,[2−6] coupled with electron correlation.[7] For the study of electron correlation in most molecular systems, several powerful approximations have been developed for classical computing platforms, and these are known to provide significant speedups compared to exponentially scaling full-configuration interaction calculations. Indeed, chemical accuracy may be obtained for many systems using the well-known CCSD(T) method[8] that has an associated scaling cost of $O(N^{6-7})$, where N represents the number of electrons.

More recently, algorithms to solve electron correlation problems in small molecular systems have been implemented on quantum hardware devices using trapped atomic ions, photons, nuclear spins, quantum dots, Rydberg atoms, and superconducting circuits.[9−20] The mapping of most electron correlation problems to quantum hardware is facilitated by the Jordan−Wigner, parity, or Bravyi−Kitaev transformations,[21−23] where a product of Fermionic creation and annihilation operators are transformed to a chain of Pauli spin operators.

In contrast, the intrinsic spin statistics of quantum nuclear dynamics problems, arising from the permutation symmetries of the wavefunctions that describe the constituent nuclear degrees of freedom, do not play a role under conditions prevalent in biological, materials, and atmospheric systems, such as hydrogen transfer reactions under ambient conditions. As a result, most such quantum dynamics studies are currently constructed on classical computing platforms using basis sets and on grids. Furthermore, many of these problems are known to display anomalous nuclear quantum effects[2,24,25] that are challenging to study on classical hardware due to the exponentially scaling computational cost of quantum dynamics with increasing degrees of freedom. Unlike several recent

Received: July 8, 2021
Published: October 25, 2021

https://doi.org/10.1021/acs.jctc.1c00688
J. Chem. Theory Comput. 2021, 17, 6713−6732

attempts on the electron correlation problem,[9−20,26−30] approximating quantum nuclear dynamics problems on quantum computing platforms has received relatively less attention.[31−37]

The primary goal of this paper is to develop a set of mapping protocols to allow the study of quantum nuclear dynamics problems on quantum hardware that do not require considering spin statistics. We provide and analyze an approximate algorithm to map exponentially scaling quantum nuclear dynamics problems on a single Born−Oppenheimer surface, onto a general class of Ising model Hamiltonians. Such Ising-type Hamiltonians may be implemented on a range of quantum computing platforms, such as ion traps,[38−42] superconducting coils,[43] Bosonic processors with photons,[44−46] solid-state devices and quantum dots inside cavities,[47−50] and Rydberg atoms.[51,52] Since quantum nuclear dynamics problems under ambient conditions do not need to be encoded using a set of Fermionic or Bosonic operators, we do not write the Ising model and molecular Hamiltonians in their respective second quantized forms. Instead, we first probe the structure of the Ising Hamiltonian matrix in its exponential scaling space of spin basis vectors. This exponential space is admittedly intractable. Yet, our analysis of the Ising Hamiltonian matrix reveals an intrinsic structure where specific blocks appear within the Ising Hamiltonian matrix, and the corresponding matrix elements are only controlled by a subset of the externally controlled field parameters that dictate the dynamics of the model. To the best of our knowledge, such a structure has never been noted, or exploited, before in the literature. This structure allows us to characterize the general class of problems that may be "computable" using such hardware systems, and in this paper, we further inspect the extent to which quantum chemical dynamics studies may be conducted on such systems, when the statistics of particle permutation need not be included.

The most significant features of the mapping algorithm are summarized in Figure 1, with a more detailed illustration

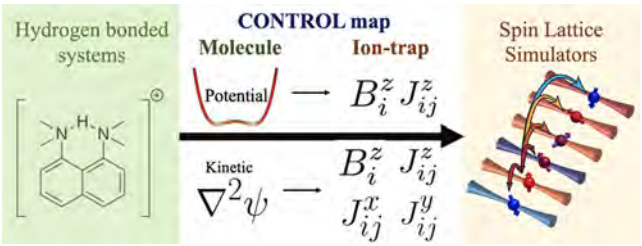

Figure 1. Critical features of our mapping algorithm. The Born−Oppenheimer potential as well as kinetic energy portions of the molecular Hamiltonian are mapped to control parameters $\{\{B_i^z\}; \{J_{ij}^x, J_{ij}^y, J_{ij}^z\}\}$ of an Ising-type spin-lattice simulator.

provided in Figure 2. An example of a quantum nuclear problem is shown in Figure 2a and also in Figure 1 (left). Here, we depict a system containing a short-strong hydrogen bond with anharmonic vibrational behavior along the donor−acceptor axis. This problem is prototypical and is representative of a broad range of systems that occur during hydrogen transfer reactions[2] and in hydrogen-bonded systems that are known to have significance in many critical processes.[1] We precompute the Born−Oppenheimer potential using electronic structure calculations and obtain a discrete version of the quantum nuclear Hamiltonian. To map this Hamiltonian onto a spin-lattice Ising-type model, the key insights in this paper are as follows: (i) A projected subspace of a specific unitary transformation of the diagonal elements of the quantum nuclear Hamiltonian (related to the Born−Oppenheimer potential) maps to and defines the local magnetic fields applied on each lattice site of an Ising model Hamiltonian. (ii) A similarly projected subspace of a related unitary transformation of the off-diagonal elements of the quantum nuclear Hamiltonian (related to the nuclear kinetic energy operator) defines and is mapped onto the intersite coupling terms in the Ising model. These features of our map are highlighted in Figure 1. Importantly, we do not use a quantum circuit model. Instead, the matrix elements of the nuclear Hamiltonian that describe the molecular dynamics, inform the choice of local magnetic fields applied on each lattice site and laser pulse intensities that dictate the intersite coupling, and govern the dynamics of the ion-trap quantum computing platform. In this manner, we provide a direct map of the two quantum systems. Thus, we take a critical step toward solving quantum nuclear dynamics problems, and more generally problems that may not obey Fermi statistics, by mapping them to Ising-type Hamiltonians realizable on ion-trap quantum hardware.

This paper is organized as follows: In Section II, we inspect the block structure of the Ising Hamiltonian, which informs the general class of problems that may be computable on hardware architectures used to realize such Ising-type Hamiltonians. Following this, we then introduce the quantum nuclear Hamiltonian matrix on a single Born−Oppenheimer surface in Section III and a class of Givens rotation[53]-based matrix transformations in Section III.I to represent the quantum nuclear Hamiltonian matrix in a form that is commensurate with the transformed form of the Ising model Hamiltonian in Section II. This transformation leads to our approximate mapping protocol that is outlined in Section IV. Numerical results for the anharmonic molecular vibrations of the shared proton in a symmetric short-strong hydrogen-bonded system are provided in Section V. These include explicit numerical propagation of both the molecular dynamics problem and the spin-lattice dynamics governed by Ising-type Hamiltonian, where the Ising Hamiltonian parameters are chosen based on the mapping protocol in Section IV. The results match exactly for the case of three qubits, and error estimates beyond three qubits are given in Section IV. Conclusions are given in Section VI. Technical aspects of the discussion are further supported through a set of appendices.

II. BLOCK STRUCTURE OF ISING-TYPE HAMILTONIAN MATRICES OBTAINED FROM APPROPRIATE CLASSIFICATION OF THE COMPUTATIONAL BASIS

Ising-type Hamiltonians can be implemented on a range of available quantum computing platforms,[38,39,43−52] which makes these one of the most commonly used quantum computing models today.[39,54] However, for specificity, we will illustrate our mapping protocols for ion-trap-based quantum architectures, where ions form defect-free arrangements and can support quantum coherence times longer than 10 min.[55] Interactions between ions map to interactions between effective quantum spin states and quantum-harmonic-oscillator bath states—each of which can be precisely controlled and programmed using laser light.[56] Site-resolved detection of

https://doi.org/10.1021/acs.jctc.1c00688
J. Chem. Theory Comput. 2021, 17, 6713−6732

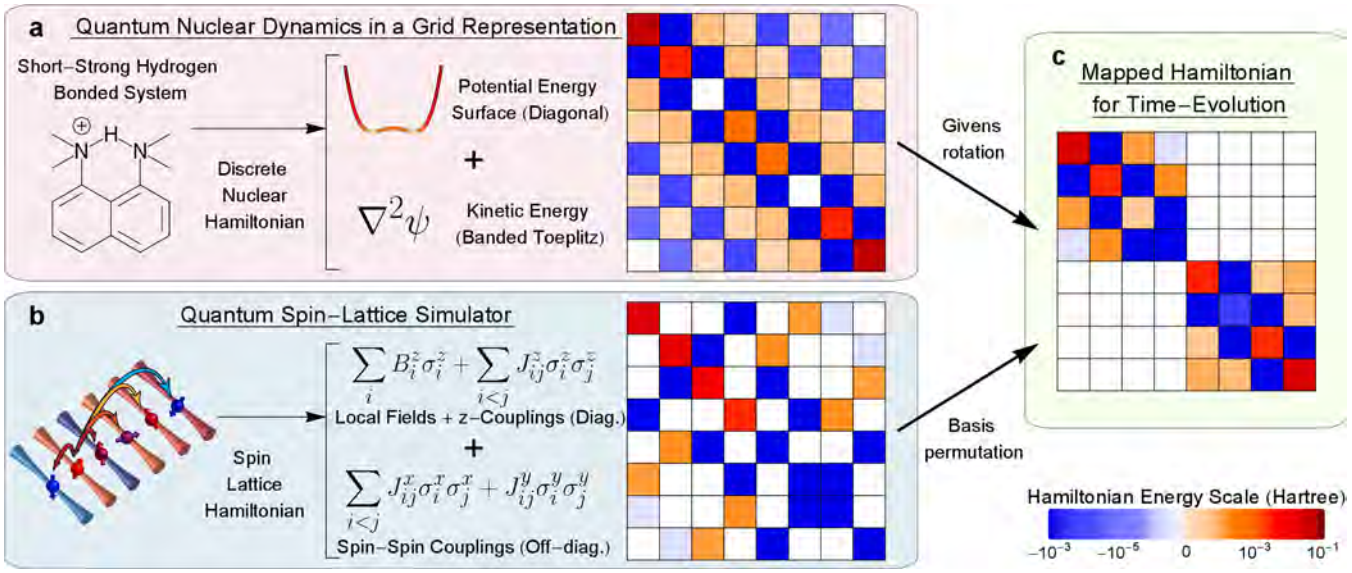

Figure 2. Algorithm that converts the Born−Oppenheimer potential surface and kinetic energy terms in a quantum nuclear problem to a set of controllable parameters and facilitates the dynamical evolution of quantum states in an ion trap. Box (a) shows the Born−Oppenheimer potential and kinetic energies for a short-strong hydrogen-bonded system. This system Hamiltonian is mapped onto an ion trap quantum simulator shown in box (b). Discrete representation of the nuclear Hamiltonian and appropriate rotations yield ion-trap parameters $\{\{B_i^z\}; \{J_{ij}^x, J_{ij}^y, J_{ij}^z\}\}$ to determine the Ising model used to control the dynamics of lattice spin states. Also see Figure 1.

each ion's spin state can be achieved with near-unit fidelity.[57] These features have made trapped ions the leading platform for establishing atomic frequency standards[58] and one of the leading candidates for performing quantum simulations and quantum computations on such interacting spin systems.[39,59−64]

For ion-trap quantum hardware, the generalized Ising Hamiltonian is represented by a spin-lattice of qubits, where (a) the energy gap between the states at each qubit, i, and their relative orientations, are controlled by local effective magnetic fields, $\{B_i^x, B_i^y, B_i^z\}$, and (b) the spin−spin coupling between different lattice sites, i and j, is controlled using laser pulses, also spatially nonisotropic, and represented as $\{J_{ij}^x, J_{ij}^y, J_{ij}^z\}$. Thus, the most general Hamiltonian achievable within the ion trap quantum hardware at low temperatures is

$$\mathcal{H}_{IT} = \sum_{\gamma} \sum_{i=1}^{N-1} \sum_{j>i}^{N} J_{ij}^{\gamma} \sigma_i^{\gamma} \sigma_j^{\gamma} + \sum_{\gamma} \sum_{i=1}^{N} B_i^{\gamma} \sigma_i^{\gamma} \tag{1}$$

where $\gamma \in (x, y, z)$ and N is the number of qubits (or ion sites). The quantities $\{\sigma_i^{\gamma}\}$ are the Pauli spin operators acting on the i^{th} lattice site along the γ-direction of the Bloch sphere. It is critical to note that the expression above is more general than that commonly used in condensed matter physics and quantum chemistry, where only nearest-neighbor interactions are considered. In fact, the set of programmable Ising-type Hamiltonians on an ion trap quantum computer depicts a complete graph that connects all qubits in a spin-lattice system with programmable interactions.[65] This aspect is completely captured in eq 1. Furthermore, a critical aspect that differentiates a quantum computer evolving according to eq 1 from a quantum simulator is one where the quantum computer can precisely address and control all $\{J_{ij}^{\gamma}\}$ values, whereas a quantum simulator programs a single functional dependence involving a $\{J_{ij}^{\gamma}\}$, thus resulting in a reduced set of controllable parameters.[39,65,66]

In this paper, we map the Born−Oppenheimer nuclear Hamiltonian to eq 1, thus allowing the two quantum systems to undergo analogous quantum dynamics. Toward this, the parameters $\{B_i^{\gamma}; J_{ij}^{\gamma}\}$ are "programmed" as per the elements of the classically determined Born−Oppenheimer nuclear Hamiltonian matrix. To arrive at such a map, we first examine the intrinsic symmetries that are present within such generalized Ising Hamiltonians.

The ion-trap Hamiltonian, $\mathcal{H}_{IT}$, is naturally represented in a basis of 2^N spin states, where, for example, $\{|\uparrow\uparrow\rangle, |\uparrow\downarrow\rangle, |\downarrow\uparrow\rangle, |\downarrow\downarrow\rangle\}$ form a basis for a two-qubit system. These now provide us with a "computational basis" with programmable handles, $\{B_i^{\gamma}; J_{ij}^{\gamma}\}$. To gauge the set of mappable problems, we introduce a general set of permutations on the computational basis vectors to reveal a novel block structure of the Ising Hamiltonian matrix. Specifically, the 2^N spin states are partitioned into two sets that are created by the span of even and odd total spin raising operators. Toward this, the basis vectors created using an even number of lattice-site spin raising operators $\{S_i^+\}$ acting on the full down-spin state, $|2^N - 1\rangle \equiv |11\cdots\rangle \equiv |\downarrow\downarrow\cdots\rangle$, yield the set $\{|\downarrow\downarrow\cdots\rangle; S_i^+ S_j^+ |\downarrow\downarrow\cdots\rangle; S_i^+ S_j^+ S_k^+ S_l^+ |\downarrow\downarrow\cdots\rangle; \cdots\}$ that is grouped as part of one block of the ion-trap Hamiltonian. See the set of vectors in Figure 3b, and the bottom left row of Figure 4, where this idea is illustrated for a three-qubit system. For the notation in this paper, we have used the binary representation $|11\cdots\rangle$ for spin state $|\downarrow\downarrow\cdots\rangle$ and the corresponding integer representation $|2^N - 1\rangle$ obtained from the bit-sequence encoded in $|11\cdots\rangle$.

Similarly, the states obtained using an odd number of raising operators $\{S_i^+ |\downarrow\downarrow\cdots\rangle; S_i^+ S_j^+ S_k^+ |\downarrow\downarrow\cdots\rangle; \cdots\}$ are grouped into a second block and are shown in Figure 3a and on the bottom right row of Figure 4.

https://doi.org/10.1021/acs.jctc.1c00688
J. Chem. Theory Comput. 2021, 17, 6713−6732

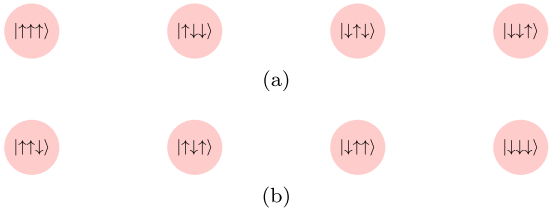

Figure 3. 2^N spin (computational) basis states partitioned into (a) the span of odd powers of the total spin raising operator acting on the down-spin state $\{\mathbf{S}^{+^{2n-1}}|\downarrow\downarrow\cdots\rangle\}$ and (b) the span of even powers of the total spin raising operator acting on the down-spin state $\{\mathbf{S}^{+^{2n}}|\downarrow\downarrow\cdots\rangle\}$. This partitioning is illustrated here for the case of three qubits and leads to a block form of H_{IT} as illustrated in Figure 4.

Thus, the two sets independently span $\{\mathbf{S}^{+^{2n}}|\downarrow\downarrow\cdots\rangle\}$ and $\{\mathbf{S}^{+^{2n-1}}|\downarrow\downarrow\cdots\rangle\}$, where $\mathbf{S}^+$ is the total spin raising operator. When the spin basis vectors are partitioned in this manner, the Ising Hamiltonian in eq 1 separates into the block structure that is illustrated in Figure 4 for a three-qubit system. Specifically, the matrix that determines the time evolution of the hardware system separates into two diagonal blocks that can only be coupled by turning on $\{B_i^x; B_i^y\}$, and this is shown in Figure 4 as part of the gray square. Thus, eliminating these $\{B_i^x; B_i^y\}$ fields would yield two separate diagonal blocks allowing the treatment of systems that may have a similar block structure. Similarly, the off-diagonal matrix elements within each diagonal block are determined by the laser field parameters, $\{J_{ij}^x; J_{ij}^y\}$. While the structure derived here is completely general, it is illustrated in Figure 4 for a three-qubit system. The diagonal elements of the matrix, not shown in Figure 4 to maintain clarity, contain linear combinations of $\{B_i^z; J_{ij}^z\}$.

For a larger number of qubits, the block structure has a recursive form, and this aspect is further elaborated in Appendix A. This block form of the Ising-type Hamiltonian and the associated structure in Figure 4 are a significant general result in this paper, and as we find below, this analysis is critical toward mapping arbitrary problems.

III. GRID-BASED QUANTUM NUCLEAR HAMILTONIAN COMPUTED ON CLASSICAL HARDWARE

The quantum nuclear Hamiltonian for the molecular system, $\mathcal{H}^{\mathrm{Mol}}$, is constructed on classical hardware, for the purpose of this paper. In the coordinate representation with basis elements, $\{|x\rangle\}$, the Hamiltonian matrix elements are given by

$$\langle x|\mathcal{H}^{\mathrm{Mol}}|x'\rangle = K(x, x') + V(x)\delta(x - x') \tag{2}$$

For local potentials, the potential energy operator, $\hat{V}$, is diagonal in the coordinate representation. The expression in

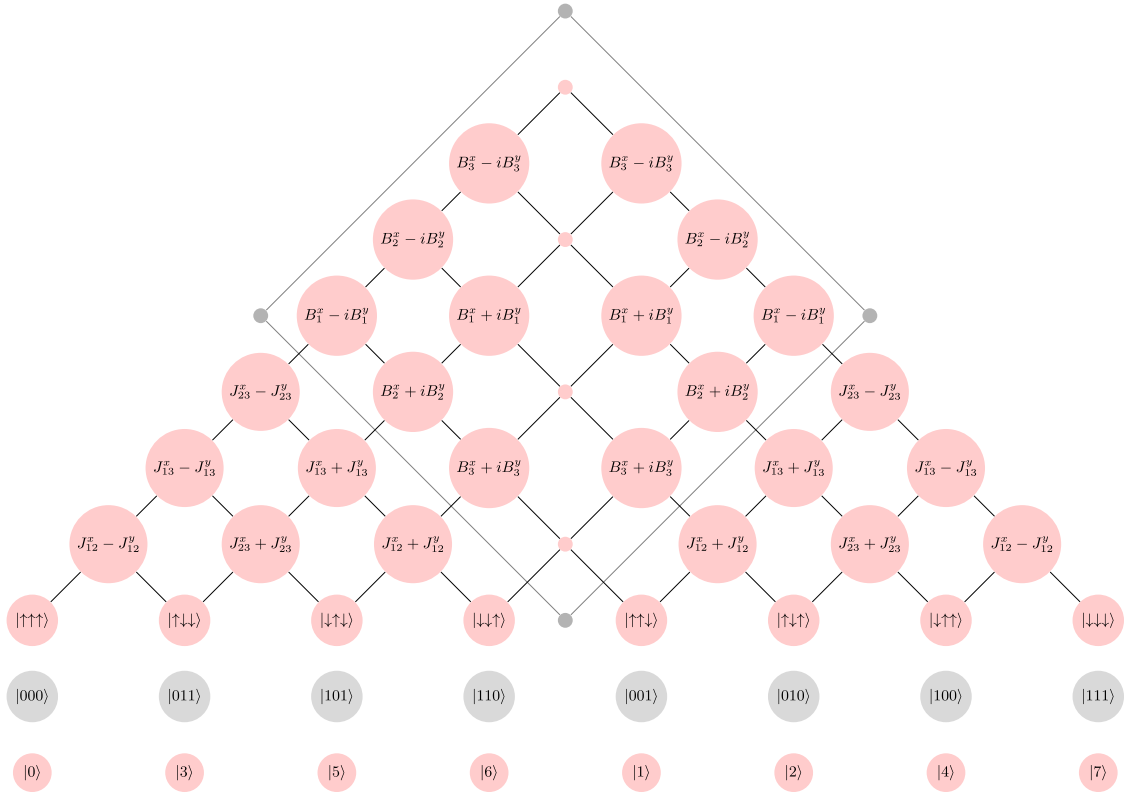

Figure 4. Upper triangular part (excluding the diagonal) of the Ising Hamiltonian, $\mathcal{H}_{IT}$ (eq 1), in the permuted computational basis illustrated for a three-qubit system. Spin (computational) basis state kets, along with their corresponding binary and integer representations, are presented at the base of the figure. These states are partitioned into odd, $\{\mathbf{S}^{+^{2n-1}}|\downarrow\downarrow\cdots\rangle\}$, and even, $\{\mathbf{S}^{+^{2n}}|\downarrow\downarrow\cdots\rangle\}$, spans of the total spin raising operators. The interaction between any two states, $|i\rangle$ and $|j\rangle$, is the ij^{th} matrix element of the ion trap Hamiltonian. For example, $\langle\uparrow\downarrow\uparrow|\mathcal{H}_{IT}|\downarrow\downarrow\downarrow\rangle \equiv [J_{13}^x - J_{13}^y]$. The off-diagonal block that couples the vectors obtained from the odd, $\{\mathbf{S}^{+^{2n-1}}|\downarrow\downarrow\cdots\rangle\}$, and even, $\{\mathbf{S}^{+^{2n}}|\downarrow\downarrow\cdots\rangle\}$, spans of the total spin raising operators are marked by the gray square.

https://doi.org/10.1021/acs.jctc.1c00688
J. Chem. Theory Comput. 2021, 17, 6713−6732

eq 2 yields a continuous representation, and in practice, the matrix and the corresponding vectors that the matrix acts on are represented on a discretized Cartesian grid. In this case, the Dirac delta function above is replaced by the Kronecker delta. The potential energy in the above equation is obtained from electronic structure calculations that may also be performed on quantum hardware, independently, in future.

The kinetic energy operator may be approximated in a number of ways. One approach is to recognize that this operator is diagonal in the momentum representation, and hence fast Fourier transforms are commonly employed.[67] In this paper, we employ an analytic banded Toeplitz distributed approximating functional (DAF)[68,69] representation for the grid representation of the kinetic energy operator in eq 2

$$K(x, x') = K(|x - x'|) = \frac{-\hbar^2}{4m\sigma^3\sqrt{2\pi}}\exp\left\{-\frac{(x - x')^2}{2\sigma^2}\right\} \sum_{n=0}^{M_{\mathrm{DAF}}/2}\left(\frac{-1}{4}\right)^n \frac{1}{n!} H_{2n+2}\left(\frac{x - x'}{\sqrt{2}\,\sigma}\right) \tag{3}$$

The banded Toeplitz representation of the DAF approximation for the kinetic energy operator, where the property of its matrix elements, $K_{ij} \equiv K(|i - j|)$, has a critical role in reducing the nuclear Hamiltonian to the form of $\mathcal{H}_{IT}$, depicted in Figure 4. This is further elaborated in the following section. In eq 3, $H_{2n+2}\left(\frac{x-x'}{\sqrt{2}\sigma}\right)$ are the even-order Hermite polynomials that only depend on the spread separating the grid basis vectors, $|x\rangle$ and $|x'\rangle$, and M_{DAF} and σ are parameters that together determine the accuracy and efficiency of the resultant approximate kinetic energy operator. Appendix D provides a brief summary of the DAF approach for approximating a function in general.

III.I. Unitary Transformations That Yield the Block Structure of the Nuclear Hamiltonian, for Symmetric Potentials, to Make These Commensurate with and Mappable to the Spin-Lattice Hamiltonian, $\mathcal{H}_{IT}$. The nuclear Hamiltonian, $\mathcal{H}^{\mathrm{Mol}}$ from eq 2, has a banded Toeplitz structure due to the kinetic energy being expressed in terms of DAFs. In general, the Hamiltonian in eq 2 represents a multidimensional quantum dynamics problem, where the number of dimensions directly corresponds to the number of nuclear degrees of freedom. In this paper, we examine the map between the Hamiltonian in eq 2 for symmetric one-dimensional potentials and the Ising model Hamiltonian discussed in Section II. Routes from here to unsymmetric potentials and to problems in higher dimensions will be considered as part of future publications. In the proton transfer problem considered here, the one-dimensional potential energy surface along the hydrogen transfer axis, $V(x)$ in eq 2, is a symmetric double well owing to the isoenergetic donor and acceptor sites arising from the symmetry of the system (Figure 2a). We exploit the symmetric structure of the potential and the Toeplitz structure of the kinetic energy operator to construct a unitary transformation that block-diagonalizes the nuclear Hamiltonian.

The unitary transform that leads to the block diagonalization of the nuclear Hamiltonian, similar to the structure of the Ising Hamiltonian, can be expressed as a product of Givens rotations. The effect of the Givens rotations on the grid basis states is to create superposition states of the symmetric grid basis states. To explain this, we introduce a uniform one-dimensional set of 2^N grid points, $\{|x_i\rangle\}$, such that the Givens-transformed grid basis, $\{|\tilde{x}_i\rangle\}$, may be represented as

$$|\tilde{x}_i\rangle \equiv \frac{1}{\sqrt{2}}[|x_i\rangle + |x_{n-i}\rangle], \quad 0 \le i < (n+1)/2 \tag{4}$$

$$\equiv \frac{1}{\sqrt{2}}[|x_i\rangle - |x_{n-i}\rangle], \quad (n+1)/2 \le i \le n \tag{5}$$

where $n = 2^N - 1$. The grid basis and the Givens-transformed grid basis, for a three-qubit system, are represented on the left columns of Figure 5. Equations 4 and 5 form two mutually

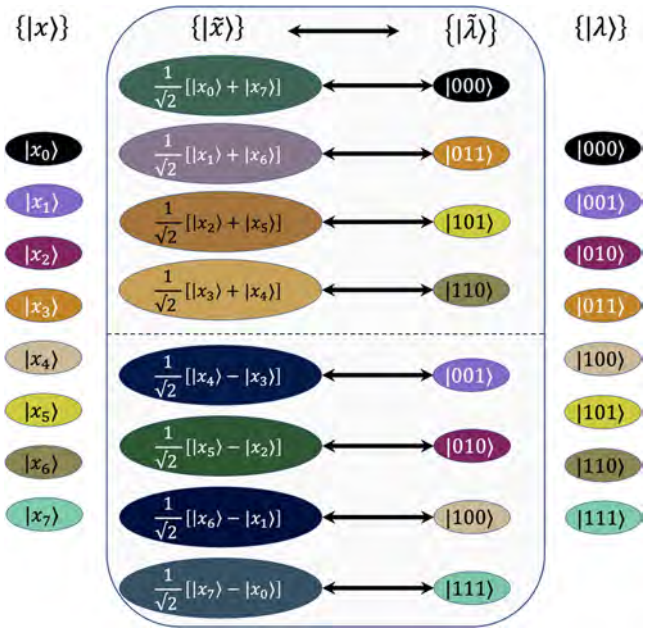

Figure 5. Illustration of the mapping of the Givens-transformed grid basis state representation, $|\tilde{x}\rangle$ (eq 5), for the discrete quantum nuclear Hamiltonian to the permuted computational basis state representation, $|\tilde{\lambda}\rangle$ (Section II), for the Ising model Hamiltonian. The respective basis states map shown here for the case of three qubits holds true and can be generalized to an arbitrary number of qubits. The dashed line in the middle separates the two blocks of each Hamiltonian.

orthogonal subspaces and are represented in the top and bottom portions of Figure 5, separated by the dashed line. These subspaces diagonalize the nuclear Hamiltonian for symmetric potentials. This process is illustrated for a three-qubit system (2^3-grid points) in Figure 6.

The il^{th} matrix element of the resultant molecular Hamiltonian in the Givens-transformed grid basis is explicitly written as

$$\tilde{\mathcal{H}}^{\mathrm{Mol}}_{il} = \frac{1}{2}(\mathcal{H}^{\mathrm{Mol}}_{i,l} + \alpha_l\mathcal{H}^{\mathrm{Mol}}_{i,n-l} + \alpha_i\mathcal{H}^{\mathrm{Mol}}_{n-i,l} + \alpha_i\alpha_l\mathcal{H}^{\mathrm{Mol}}_{n-i,n-l}) \tag{6}$$

where $\alpha_i = \mathrm{sgn}[i - (n/2)]$. The elements of the diagonal blocks of $\tilde{\mathcal{H}}^{\mathrm{Mol}}$ (matrix on the right in Figure 6) are obtained from eq 6 as

https://doi.org/10.1021/acs.jctc.1c00688
J. Chem. Theory Comput. 2021, 17, 6713−6732

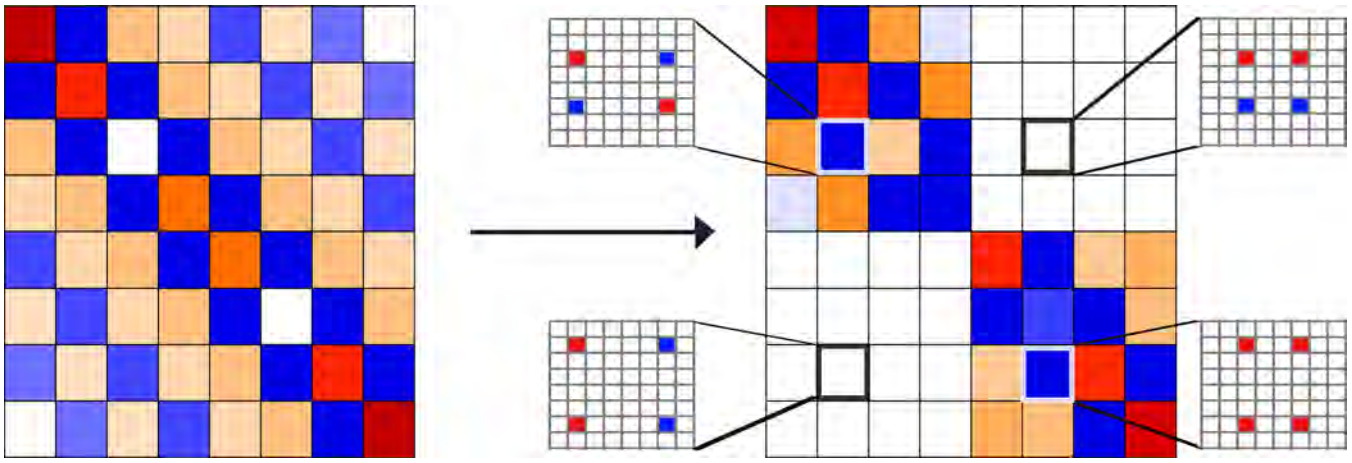

Figure 6. Illustration of the block diagonalization of the nuclear Hamiltonian, as captured by eq 6. (Left) Original Hamiltonian, $\mathcal{H}^{\mathrm{Mol}}$; (right) transformed $\tilde{\mathcal{H}}^{\mathrm{Mol}}$. On the right side, specific matrix elements from each block of $\tilde{\mathcal{H}}^{\mathrm{Mol}}_{il}$ are highlighted to illustrate eqs 7 and 8. These highlighted elements of $\tilde{\mathcal{H}}^{\mathrm{Mol}}_{il}$ are obtained by combining elements of $\mathcal{H}^{\mathrm{Mol}}$, as per eq 6, and these are marked using red and blue squares in zoomed-in representations of matrix elements in $\mathcal{H}^{\mathrm{Mol}}$. Blue (negative) and red (positive) indicate the phase of the corresponding elements of $\mathcal{H}^{\mathrm{Mol}}$, as obtained from α_i in eqs 6−8.

$$\tilde{\mathcal{H}}^{\mathrm{Mol}}_{il} = \frac{1}{2}(\mathcal{H}^{\mathrm{Mol}}_{i,l} + \alpha_i\mathcal{H}^{\mathrm{Mol}}_{i,n-l} + \alpha_i\mathcal{H}^{\mathrm{Mol}}_{n-i,l} + \mathcal{H}^{\mathrm{Mol}}_{n-i,n-l}) = [K(x_i, x_l) + \alpha_i K(x_i, x_{n-l})] + \frac{1}{2}[V(x_i) + V(x_{n-l})]\delta_{i,l} \tag{7}$$

The elements of the unitary transform, α_i, are, in fact, the characters of the C_s point group. The right-hand side of the above equation, therefore, represents a symmetry-adapted transformation of the nuclear Hamiltonian, and the term $(1/2)\ [V(x_i) + V(x_{n-i})]$ symmetrizes the potential energy surface in one dimension. By extension, for the elements of the off-diagonal blocks of $\tilde{\mathcal{H}}^{\mathrm{Mol}}$ in Figure 6, $\alpha_l = -\alpha_i$ and

$$\tilde{\mathcal{H}}^{\mathrm{Mol}}_{il} = \frac{1}{2}(\mathcal{H}^{\mathrm{Mol}}_{i,l} - \alpha_i\mathcal{H}^{\mathrm{Mol}}_{i,n-l} + \alpha_i\mathcal{H}^{\mathrm{Mol}}_{n-i,l} - \mathcal{H}^{\mathrm{Mol}}_{n-i,n-l}) = \frac{1}{2}[V(x_i) - V(x_{n-l})]\delta_{i,n-l} \tag{8}$$

where the kinetic energy contribution is identically zero purely due to the Toeplitz nature of eq 3, and only the antisymmetric portion of the potential, $(1/2)\ [V(x_i) - V(x_{n-l})]$, contributes to the antidiagonal part of $\tilde{\mathcal{H}}^{\mathrm{Mol}}$. Thus, for symmetric potentials such as those considered here, eq 8 is identically zero. This observation will become useful when we generalize the approach presented here, first to general potentials and then to problems of higher dimensionality in future publications.

IV. MAPPING PROTOCOL FOR QUANTUM CHEMICAL DYNAMICS

The structure of the ion-trap Hamiltonian constrains the class of mappable problems. These constraints dictate the accuracy with which quantum chemical dynamics simulations can be performed on an ion-trap system given by eq 1. To summarize our discussion thus far (see Figure 5), we began with a computational basis $|\lambda\rangle$ used to describe the Ising Hamiltonian, $\mathcal{H}_{IT}$ in eq 1, and the grid basis $|x\rangle$ used to represent the quantum nuclear Hamiltonian, $\mathcal{H}^{\mathrm{Mol}}$ in eq 2. In the interest of matching the structures of the two Hamiltonians, we first obtained a permuted computational basis: $|\lambda\rangle \rightarrow |\tilde{\lambda}\rangle$ (Section II, and also summarized on the right side of Figure 5) and a unitary (Givens) transformed quantum nuclear basis: $|x\rangle \rightarrow |\tilde{x}\rangle$ (Section III.I). In doing so, our goal becomes

$$\langle\tilde{x}|\,\mathcal{H}^{\mathrm{Mol}}|\widetilde{x'}\rangle \leftrightarrow \langle\tilde{\lambda}|\,\mathcal{H}_{\mathrm{IT}}|\widetilde{\lambda'}\rangle \tag{9}$$

where we first introduce a map between the transformed quantum nuclear wavefunction bases and the permuted computational bases that represent the Ising spin-lattice system as

$$|\tilde{x}\rangle \Leftrightarrow |\tilde{\lambda}\rangle \tag{10}$$

This map is illustrated within the central box in Figure 5, where the left side of the central box represents the Givens-transformed grid basis and the right side represents the permuted computational basis. Furthermore, the mapped basis states are separated into blocks by a dashed horizontal line. For the molecular Hamiltonian, the coupling across these blocks is identically zero for symmetric potentials, while for the Ising Hamiltonian, the coupling across these blocks is identically zero when the terms B^x_i and B^y_i are eliminated from eq 1 (see Figure 4). The effectiveness of the maps in eqs 9 and 10 will essentially dictate the accuracy to which the dynamics captured within the ion-trap quantum simulator controlled by an Ising Hamiltonian accurately predicts the quantum nuclear dynamics.

In this section, we will show that, due to the structure of the Hamiltonians discussed in the previous sections, the diagonal and off-diagonal elements of each individual diagonal block of mappable Hamiltonians, such as eq 2, are Hadamard-transformed to provide $\{B^z_i;\ J^z_{ij}\}$ and $\{J^x_{ij};\ J^y_{ij}\}$, respectively. As a consequence of the discussion in Section III.I, both Hamiltonians, eqs 1 and 2, by construction, take the form depicted in Figure 2c and the right side of Figure 6, respectively. Our quantum nuclear dynamics test case that will be mapped to the aforementioned Ising Hamiltonian (Section

https://doi.org/10.1021/acs.jctc.1c00688
J. Chem. Theory Comput. 2021, 17, 6713−6732

V) exploits the block structure discussed above, and we illustrate the map by studying a symmetric hydrogen-bonded system displayed in Figure 2a, where a symmetric double-well potential is also shown. For these cases, as seen from eqs 8 and 7 and the discussion in Section II and eq A4 in Appendix A, the block structure of both the Hamiltonian matrices allows the two blocks of each Hamiltonian matrix (Ising and molecular) to be propagated independently, and, potentially on different quantum simulators, for the Ising Hamiltonian. We exploit this feature to evaluate a separate set of $\{B_i^z; J_{ij}^z\}$ values, below, for each of the two diagonal blocks of the molecular Hamiltonian, while maintaining $\{B_i^x; B_i^y\}$ to be identically zero.

IV.I. Obtaining Ion-Trap Parameters $\{B_i^z; J_{ij}^z\}$ from the Diagonal Elements of the Molecular Hamiltonian. The diagonal elements of the molecular Hamiltonian are directly mapped to those of the spin-lattice Hamiltonian after invoking the map of the unitary-transformed grid basis ($|\tilde{x}\rangle$) to the permuted computational basis ($|\tilde{\lambda}\rangle$). Each diagonal element of the molecular Hamiltonian in the transformed grid representation $\langle\tilde{x}|\,\mathcal{H}^{\mathrm{Mol}}|\tilde{x}\rangle$ is equivalent to the corresponding element of the ion-trap Hamiltonian $\langle\tilde{\lambda}|\,\mathcal{H}_{IT}|\tilde{\lambda}\rangle$ in the permuted computational basis representation. In doing so, the set of on-site and intersite coupling parameters $\{B_i^z; J_{ij}^z\}$ of the ion-trap that occur along the diagonal of $\tilde{\mathcal{H}}_{IT}$ can be evaluated. The mapping expression between the diagonal elements of the molecular Hamiltonian and the corresponding elements of the ion-trap Hamiltonian may be written as

$$\langle\tilde{x}|\,\mathcal{H}^{\mathrm{Mol}}|\tilde{x}\rangle \equiv \langle\tilde{\lambda}|\,\mathcal{H}_{IT}|\tilde{\lambda}\rangle \tag{11}$$

Using eq 7 and eq 1, for the left and right sides of eq 11, we obtain

$$[K(x_i, x_i) - K(x_i, x_{n-i})] + \frac{1}{2}[V(x_i) + V(x_{n-i})] = \sum_{j=1}^{N}(-1)^{\tilde{\lambda}_j}B_j^z + \sum_{j=1}^{N-1}\sum_{k>j}^{N}(-1)^{\tilde{\lambda}_j\oplus\tilde{\lambda}_k}J_{jk}^z \quad \text{for } i < n/2 \tag{12}$$

$$[K(x_i, x_i) + K(x_i, x_{n-i})] + \frac{1}{2}[V(x_i) + V(x_{n-i})] = \sum_{j=1}^{N}(-1)^{\tilde{\lambda}_j}B_j^z + \sum_{j=1}^{N-1}\sum_{k>j}^{N}(-1)^{\tilde{\lambda}_j\oplus\tilde{\lambda}_k}J_{jk}^z \quad \text{for } i > n/2 \tag{13}$$

where $\oplus$ on the right side denotes the addition modulo 2 and $\tilde{\lambda}_j$ is the jth bit of the bit representation of $|\tilde{\lambda}\rangle$ with values 0 or 1 for up- or down-spin, respectively, as shown in Figure 3 and Figure 4.

Our goal is to use the diagonal elements of $\tilde{\mathcal{H}}^{\mathrm{Mol}}$ to obtain ion-trap parameters $\{B_i^z, J_{ij}^z\}$. The expressions needed for this purpose are derived from eqs 12 and 13, and a detailed discussion on this map is provided in Appendix B. In summary, we show in Appendix B that the ion-trap control parameters $\{B_i^z; J_{ij}^z\}$ are specific Hadamard transforms of $\langle\tilde{x}|\,\mathcal{H}^{\mathrm{Mol}}|\tilde{x}\rangle$, that is

$$\langle\tilde{x}|\,\mathcal{H}^{\mathrm{Mol}}|\tilde{x}\rangle \xrightarrow{\text{Hadamard}} \{B_i^z; J_{ij}^z\} \tag{14}$$

This is a particularly key result in this paper, since the Hadamard transforms, like Fourier transforms,[70] are unitary and hence the ion-trap parameters, $\{B_i^z; J_{ij}^z\}$, are Walsh–Hadamard-transform[71] components of $\langle\tilde{x}|\,\mathcal{H}^{\mathrm{Mol}}|\tilde{x}\rangle$. However, while this map is general for arbitrary number of qubits, we will also describe in Appendix B that the linear transformations between $\langle\tilde{x}|\,\mathcal{H}^{\mathrm{Mol}}|\tilde{x}\rangle$ and $\{B_i^z; J_{ij}^z\}$, in eqs 11, 12 and 13, are rank-deficient and hence error estimates are also presented in Appendix B that apply for arbitrary number of qubits.

Before we conclude this section, we note that the map in eqs 12 and 13 may be used for the potential-free particle in a box case by eliminating the potential leading to

$$[K(x_i, x_i) - K(x_i, x_{n-i})] = \sum_{j=1}^{N}(-1)^{\tilde{\lambda}_j}B_j^z + \sum_{j=1}^{N-1}\sum_{k>j}^{N}(-1)^{\tilde{\lambda}_j\oplus\tilde{\lambda}_k}J_{jk}^z \quad \text{for } i < n/2 \tag{15}$$

$$[K(x_i, x_i) + K(x_i, x_{n-i})] = \sum_{j=1}^{N}(-1)^{\tilde{\lambda}_j}B_j^z + \sum_{j=1}^{N-1}\sum_{k>j}^{N}(-1)^{\tilde{\lambda}_j\oplus\tilde{\lambda}_k}J_{jk}^z \quad \text{for } i > n/2 \tag{16}$$

V. PERFORMANCE OF THE MAPPING PROTOCOL FOR A SYMMETRIC HYDROGEN-BONDED SYSTEM

We examine the map by simulating the quantum dynamics of the molecular system and the ion-trap dynamics, on classical hardware, independently. In doing so, we study the time evolution of the initial wavepacket states prepared in the respective permuted basis representations for the molecular and Ising model Hamiltonians. As stated, the parameters in the Ising Hamiltonian are determined, and thus controlled, by the precomputed matrix elements of the molecular Hamiltonian. The specific intramolecular proton transfer problem considered here is that in the protonated 1,8-bis-(dimethylamino) naphthalene ($DMANH^+$) system shown in Figure 7a. The DMAN molecule has an extremely large proton affinity of 242 kcal/mol,[72] with $DMANH^+$ pK_a value in the range of 12.1–12.3.[73] As a result, the system is one of the most frequently investigated proton sponges. The NHN^+ hydrogen bond in proton sponges is attractive from the point of view of both the nature of the short potentially symmetric hydrogen-bond bridges,[74−77] their infrared spectroscopic behavior, and their propensity to occur in common nitrogen activation catalysts.[78,79] Thus, the $DMANH^+$ system has been frequently studied as a model for short, low-barrier hydrogen bonds that have a role in certain enzyme-catalyzed reactions. In solution, the shared proton delocalization in $DMANH^+$ is controlled by a low-barrier symmetric double-well potential, with barrier height being influenced by solvent and temperature.[80,81] In fact, the environment and variables such as solvent and temperature influence the donor–acceptor distance fluctuations, thus having a critical role in the quantum mechanical nature of the shared proton. The effect of these donor–acceptor variables is seen in Figure 7b, where we present the shared proton one-dimensional symmetric potentials (red curves on the right side of Figure 7b) for a

https://doi.org/10.1021/acs.jctc.1c00688
J. Chem. Theory Comput. 2021, 17, 6713−6732

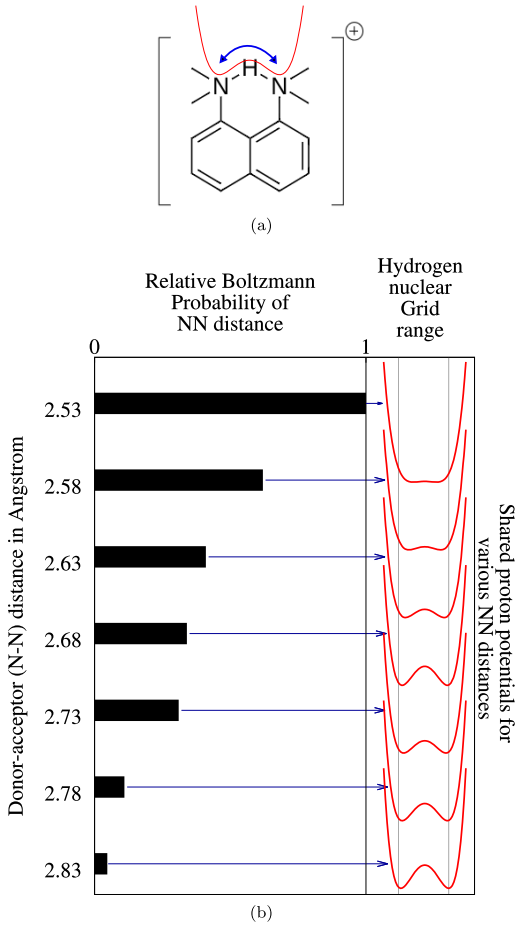

Figure 7. (a) Molecular geometry for $DMANH^+$ with the shared proton potential surface shown in red. The quantum mechanical nature of the shared proton allows it to be simultaneously present in both wells, and here, we use eq 1 to simulate the behavior of this shared proton throughout mapping protocol in eq 9. (b) Change in double-well potential (and barrier height) as a function of donor−acceptor (N−N) distance. The bar heights show the classical Boltzmann population for each N−N distance.

range of donor−acceptor distances (left vertical axis in Figure 7b) with significant classical Boltzmann populations (black horizontally placed histograms in Figure 7b) at room temperature. Clearly, the barrier heights separating the minima in the red curves as well as respective minimum-energy positions are sensitive to donor−acceptor fluctuations and influence the spectroscopic properties of such hydrogen-bonded systems.[82,83] To emphasize this, in Figure 7b, the light gray vertical lines are positioned to approximately coincide with the minimum-energy values for the red potential energy surface at an NN distance of 2.83 Å. As the NN distance gets smaller, the minimum-energy points get closer to each other and changes the nature of the confinement potential in the shared hydrogen nucleus. Here, the effects of all of these aspects are studied by mapping the quantum nuclear dynamics problem on multiple potential surfaces, obtained from different donor−acceptor (NN) distances, to ion-trap quantum simulators.

In the following subsections, we present the methods used to classically precompute the nuclear Hamiltonian for each of the donor−acceptor distances shown in Figure 7b and simulate the quantum nuclear dynamics on these potentials using the Ising model-based ion-trap simulators. We treat the shared proton stretch dimension within the Born−Oppenheimer limit. The nuclear Hamiltonian is determined by the ground electronic-state potential energy surface.

V.I. Precomputing the Molecular Hamiltonian ($\mathcal{H}^{\mathrm{Mol}}$ in Equation 2) on Classical Hardware. To compute the potential energy surface for the intramolecular proton transfer in the molecular system $DMANH^+$ (Figures 2a and 7a), we locate a symmetric stationary point with the shared proton at the center of the donor−acceptor axis. For the case of $DMANH^+$, this stationary point turns out to be a transition state with one imaginary frequency that is obtained from the eigenstates of the electronic structure Hessian matrix, with the vibrational mode corresponding to the intramolecular proton transfer direction. At this geometry, the shared proton is symmetrically located between the donor and acceptor nitrogen atoms. These calculations are performed using standard electronic structure methods. The level of electronic structure theory used is density functional theory with hybrid functional, B3LYP, and an atom-centered Gaussian basis set containing polarization and diffuse functions on all atoms, that is, 6-311++G(d,p). Future work will also include mapping of this Hamiltonian precomputation step onto quantum hardware. A reduced dimensional potential energy surface calculation for one-dimensional proton motion along the donor−acceptor axis is performed at the aforementioned stationary point geometry. This is also done for a set of donor−acceptor distances with significant classical Boltzmann populations as seen in Figure 7b. The potential energy surfaces are obtained on a grid defined along the donor−acceptor axis. We choose 2^N number of equally spaced grid points, symmetrically located about the grid center, and perform electronic structure calculations at these points, on a classical computing platform, at the level of theory mentioned above. The molecular Hamiltonian is computed (eq 2) and unitary-transformed to achieve a block structure according to Section III.I.

V.II. Quantum Simulation of Proton Transfer Dynamics. Given the block structure of both molecular and Ising Hamiltonians in the permuted and Givens-transformed basis representations, the initial wavepacket for the ion-trap system is chosen as a coherent linear combination of the spin basis states: $\left\{\frac{|\uparrow\uparrow\uparrow\rangle + |\downarrow\downarrow\downarrow\rangle}{\sqrt{2}}\right\}$ on a three-qubit system. Given the block structure of the Ising Hamiltonian with $\{B_i^x, B_i^y\}$ turned off, the components of this initial state, $|\uparrow\uparrow\uparrow\rangle$ and $|\downarrow\downarrow\downarrow\rangle$, are not coupled. Additionally, these states will not couple as might be the case in the presence of $B_3^x - iB_3^y$ in the off-diagonal blocks: for example, pathways such as

$$|\downarrow\downarrow\downarrow\rangle \xrightarrow{B_3^x - iB_3^y} |\uparrow\downarrow\downarrow\rangle \xrightarrow{J_{12}^x - J_{12}^y} |\uparrow\uparrow\uparrow\rangle$$

will remain unpopulated. Hence, in essence, $|\uparrow\uparrow\uparrow\rangle$ gets propagated as per the unitary evolution corresponding to the top diagonal block of the Ising Hamiltonian and $|\downarrow\downarrow\downarrow\rangle$ as per the bottom block. This critical feature allows us to treat the two separated blocks as arising from two different ion traps with two different sets of $\{B_i^\gamma; J_{ij}^\gamma\}$ parameters. Given the direct map in eq 10 between the permuted computational basis and the Givens-transformed molecular grid basis, the initial wavepacket for the molecular system is to be chosen in an analogous manner to the initial wavepacket of the ion-trap,

https://doi.org/10.1021/acs.jctc.1c00688
J. Chem. Theory Comput. 2021, 17, 6713−6732

which is $\left\{\frac{|\tilde{x}_0\rangle + |\tilde{x}_7\rangle}{\sqrt{2}}\right\}$. This essentially leads to the initial wavepacket for the quantum nuclear dynamics problem as being chosen on one end of the grid, that is, a state localized closer to one of the nitrogen atoms in Figures 2a and 7a. This choice results in the initial nuclear wavepacket being symmetrically located at either end of the Givens-transformed basis (eq 5). The spin-lattice and molecular wavepackets are then independently propagated for each potential obtained for different donor−acceptor separations and compared to gauge accuracy of the quantum simulation.

Given the recursive form of the matrix representation of the Ising Hamiltonian in eq 1, as discussed in Appendix A (see eq A4), the ion-trap hardware initial wavepacket state is directly propagated by the choice of $\{B_i^\gamma; J_{ij}^\gamma\}$ for arbitrary time segments. In this study, we do not seek experimental validation using a real ion-trap simulator but emulate the time evolution of the ion-trap system according to the Hamiltonian in eq 1 on classical hardware, using the eigenstates of the Ising Hamiltonian in Appendix A. The time-dependent probabilities resulting from the projection of the resultant time-dependent wavepacket on the computational basis, at each interval of time, is shown using dashed lines in Figures 8 and 9 for a donor−acceptor distance of

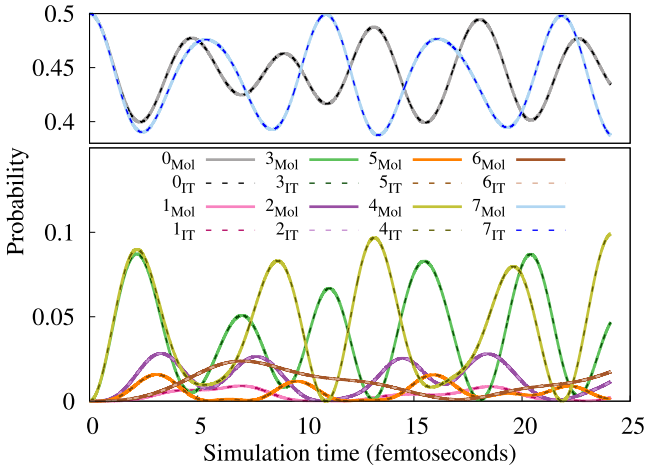

Figure 8. Dynamics of the molecular and the ion trap systems: The integer (i) depicts the projection of a propagated state onto the ith permuted spin basis state and the corresponding Givens-transformed grid basis state for the ion-trap (dashed) and the molecular system with d_{DA} = 2.53 Å (solid), respectively. Note that all propagations are conducted on classical platforms. The agreement of the quantum dynamics in both systems is exact to within numerical round-off (10^{-15}). The two rows in the figure legend represent the two sets spanned by odd and even spin raising operators, $\{S^+\}$, acting on the $|\downarrow\downarrow\cdots\rangle$ spin state (dashed) and their corresponding Givens-transformed grid basis states (solid) according to eq 10. An extended set of d_{DA} is shown in Figure 10, and results for a longer-term dynamics for the most stable structure (d_{DA} = 2.53 Å) are provided in Figure 9.

2.53 Å and for the full set of donor−acceptor distance values in Figure 10. (The donor−acceptor distance of 2.53 Å corresponds to the most stable structure, but as seen from Figure 10, there are several other geometries that are also populated (at 300K) even from a purely classical Boltzmann estimation.) Similarly, we determine the time evolution of the initial wavepacket for the molecular system using the

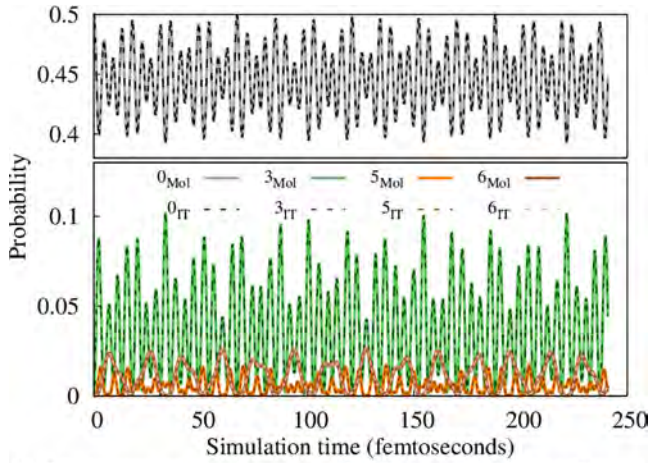

(a)Projections of the time-dependent wavepackets onto Block I vectors

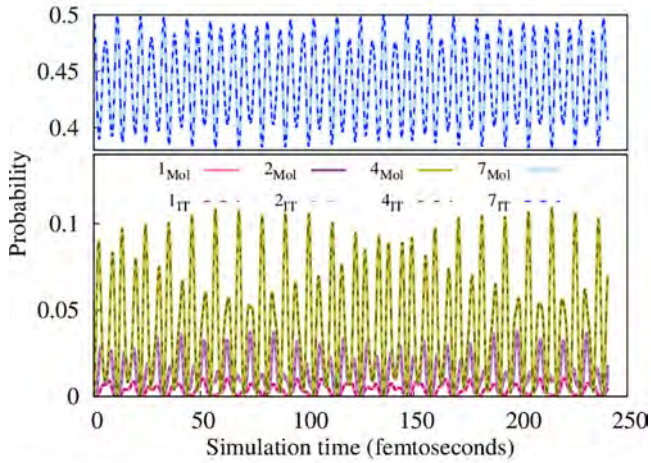

(b)Projections of the time-dependent wavepackets onto Block II vectors

Figure 9. Dynamics of the molecular system (solid) and the ion-trap system (dashed) that show their exact match to within numerical round-off (10^{-15}) over long simulation times sufficient to capture the molecular vibrational properties. Complements Figure 8. The projection of the respective time-dependent wavepackets onto basis vectors within each of the two decoupled blocks is shown separately for clarity.

eigenstates of the transformed Hamiltonian in eq 6, and the resulting probabilities from the projection of the time-dependent wavepacket on the Givens-transformed grid basis $\{|\tilde{x}\rangle\}$ are shown using solid lines in Figures 8−10. The probabilities match exactly, apart from numerical round-off error (10^{-15}), for the quantum simulation of the dynamics of the two systems. Clearly, this is also true for much longer time intervals as can be seen in Figure 9. Given the exact match between the spin-lattice dynamics and the quantum chemical dynamics, the features present in ion-trap dynamics must also exist in the chemical dynamics problem. Thus, through the isomorphism constructed above, our algorithm shows the ability to probe any entanglement that may be present in chemical systems.

VI. CONCLUSIONS AND OUTLOOK

The successful simulation of quantum nuclear dynamics on quantum hardware promises a new paradigm for studying a

https://doi.org/10.1021/acs.jctc.1c00688
J. Chem. Theory Comput. 2021, 17, 6713−6732

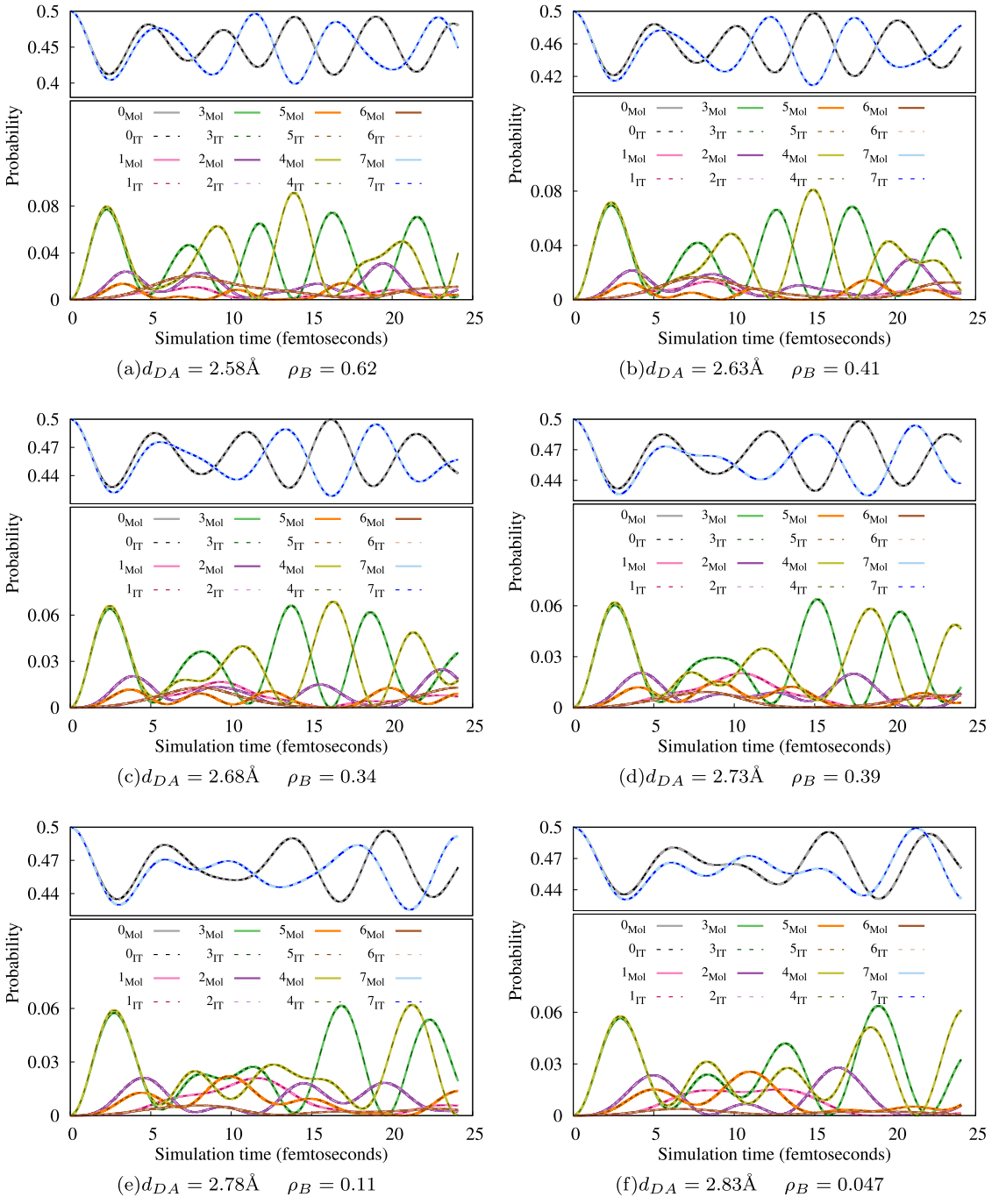

Figure 10. Similar to Figure 8 but for multiple donor−acceptor distances (d_{DA}) between the nitrogen atoms for the molecule in Figure 2a. Boltzmann populations (ρ_B) are computed at 300 K relative to the population of the configuration used in Figure 8 that has a d_{DA} value of 2.53 Å. The correlated changes in the $|0\rangle$ and $|7\rangle$ projections are clearly facilitated by components along other basis vectors, and these may have a critical role in the reactive process as a function of temperature. The fact that the ion-lattice dynamics displays the same dynamical trends provides an additional probe to complex chemical systems.

broader class of coupled electron nuclear transfer problems. In this study, we provide a general but approximate mapping procedure between a quantum chemical dynamics problem, constructed on a single Born−Oppenheimer surface, and an ion-trap quantum simulator where the dynamics is dictated by a generalized form of the Ising model Hamiltonian. The key step involved in facilitating our map is the partitioning of the coupled qubit space into two zones using only odd or even powers of the total spin raising operators that are used to generate such a coupled qubit space. Once the coupled qubit computational basis set is partitioned in such a way, the Ising model Hamiltonian reduces into a block form, thus allowing the possibility to map all problems that may be written in a similar block form. In some sense, we have also taken here the necessary steps to detail the kinds of general problems that can be solved exactly on a quantum system whose dynamics is dictated by a generalized form of the Ising model Hamiltonian. In this particular paper, though, we consider a symmetric proton transfer problem and then go on to show how such a problem can be mapped to an ion-trap system and

https://doi.org/10.1021/acs.jctc.1c00688
J. Chem. Theory Comput. 2021, 17, 6713−6732

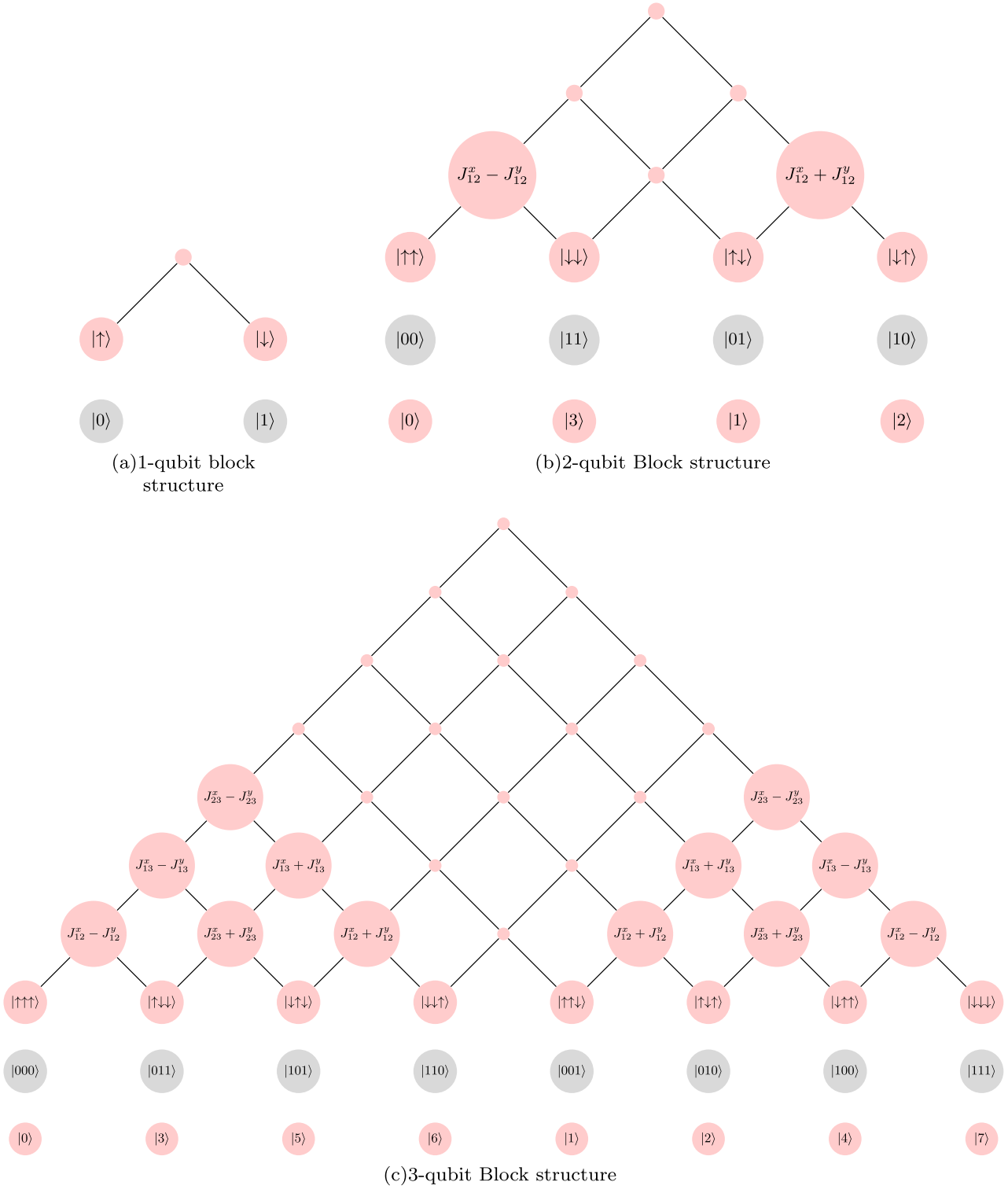

(a)1-qubit block structure

(b)2-qubit Block structure

(c)3-qubit Block structure

Figure 11. Complements Figure 4. At the base of each figure are the computational basis state kets. The interaction between any two states ($|\tilde{\lambda}_i\rangle$) and $\left(\left|\tilde{\lambda}_j\right\rangle\right)$ can be read off from the graph, by starting at the two states and following the lines to their intersection. The node at the intersection gives the interaction between the two. For example, $|2\rangle$ and $|7\rangle$ in (c) have an off-diagonal matrix element of $[J_{13}^x - J_{13}^y]$. The blank nodes are zero and show the block diagonal form of the Ising Hamiltonian when $\{B_i^x; B_i^y\}$ are set to zero.

also show that the dynamics of the two systems is identical provided the parameters of the ion trap are chosen in concert with that of the molecular system obtained from classical precomputation. We also provide error bounds for this approximate algorithm for arbitrary number of qubits.

General quantum nuclear dynamics problems, however, have unsymmetric potential energy surfaces and are generally performed in higher dimensions. This work will become critical in extending our mapping protocol to general potentials in higher dimensions, as will be considered in

https://doi.org/10.1021/acs.jctc.1c00688
J. Chem. Theory Comput. 2021, 17, 6713−6732

future publications. In addition, the next set of steps also includes inspection of nuclear wavepacket basis set dependence on the accuracy of the proposed map. Using appropriate basis sets, it may be possible to reduce the number of independent descriptors within the molecular Hamiltonian, thus tailoring the accuracy of the map according to the constraints provided in this paper.

APPENDIX A: RECURSIVE, BLOCK STRUCTURE OF THE ISING HAMILTONIAN MATRIX

The Ising Hamiltonian matrix, $\mathbf{H_N}$, for a spin-lattice system with N qubit sites, when written in the computational basis partitioned according to sets that span $\{\mathbf{S}^{+^{2n}}|\downarrow\downarrow\cdots\rangle\}$ and $\{\mathbf{S}^{+^{2n-1}}|\downarrow\downarrow\cdots\rangle\}$, may be recursively written in a blocked form as

$$\mathbf{H_N} = \begin{bmatrix} \mathbf{H_N^{D1}} & \mathbf{B_N} \\ \mathbf{B_N^\dagger} & \mathbf{H_N^{D2}} \end{bmatrix} \tag{A1}$$

Here, both the diagonal blocks $\mathbf{H_N^{D1}}$ and $\mathbf{H_N^{D2}}$, and the off-diagonal block $\mathbf{B_N}$ are recursively defined as per

$$\mathbf{H_N} = \left[\begin{array}{cc|cc} \mathbf{H_{N-1}^{D1}} + B_N^z \mathbf{I}_{2^{N-2}} + \mathbf{J}_{z,N}^1 & \mathbf{J}_{xy,N}^1 & \mathbf{B}_{N-1} & (B_N^x - iB_N^y)\mathbf{I}_{2^{N-2}} \\ \mathbf{J}_{xy,N}^{1\,T} & \mathbf{H_{N-1}^{D2}} - B_N^z \mathbf{I}_{2^{N-2}} + \mathbf{J}_{z,N}^1 & (B_N^x + iB_N^y)\mathbf{I}_{2^{N-2}} & \mathbf{B}_{N-1} \\ \hline \mathbf{B}_{N-1}^\dagger & (B_N^x - iB_N^y)\mathbf{I}_{2^{N-2}} & \mathbf{H_{N-1}^{D2}} + B_N^z \mathbf{I}_{2^{N-2}} + \mathbf{J}_{z,N}^2 & \mathbf{J}_N^2 \\ (B_N^x + iB_N^y)\mathbf{I}_{2^{N-2}} & \mathbf{B}_{N-1}^\dagger & \mathbf{J}_{xy,N}^{2\,T} & \mathbf{H_{N-1}^{D1}} + B_N^z \mathbf{I}_{2^{N-2}} + \mathbf{J}_{z,N}^2 \end{array}\right] \tag{A2}$$

where $\mathbf{I}_{2^N}$ denotes an identity matrix of size 2^N. The quantities $\mathbf{J}_{xy,N}^1$ and $\mathbf{J}_{xy,N}^2$ are matrices that appear in the recursive definition of the diagonal blocks, labeled with superscripts $\mathbf{D_1}$ and $\mathbf{D_2}$, respectively, and contain intersite coupling of the Nth spin site with the remaining $N-1$ sites. To arrive at the matrix elements belonging to $|\tilde{\lambda}\rangle\, \mathbf{J}_{xy,N}^1\, \langle\tilde{\lambda}'|$ and $|\tilde{\lambda}\rangle\, \mathbf{J}_{xy,N}^2 \langle\tilde{\lambda}'|$ in the equation above, a bitwise XOR operation is constructed between the corresponding computational bases, $|\tilde{\lambda}\rangle$ and $|\tilde{\lambda}'\rangle$. The XOR operation provides the identity of the spin sites where the computational basis vectors $|\tilde{\lambda}\rangle$ and $|\tilde{\lambda}'\rangle$ differ, that is, when the spin states are flipped between $|\tilde{\lambda}\rangle$ and $|\tilde{\lambda}'\rangle$. When the bases differ at two spin-lattice site locations, i and j, the corresponding matrix element of $\mathbf{J}_{xy,N}^1$ or $\mathbf{J}_{xy,N}^2$ is given by $J_{ij}^x \pm J_{ij}^y$. The phase preceding the J_{ij}^y values results from an XNOR operation on the i, j lattice sites discovered through the XOR operation above.

The terms, $\mathbf{J}_{z,N}^1$ and $\mathbf{J}_{z,N}^2$, in eq A2 are also defined in a similar manner. Both $\mathbf{J}_{z,N}^1$ and $\mathbf{J}_{z,N}^2$ matrices are diagonal in form. Thus, the diagonal elements of $\mathbf{H_N^{D1}}$ and $\mathbf{H_N^{D2}}$ are incremented by a linear combination of all possible intersite couplings of the Nth spin site with the remaining $N-1$ sites given by $\sum_{i=1}^{N-1}(-1)^{\tilde{\lambda}_i \oplus \tilde{\lambda}_N} J_{iN}^z$. (Also see eqs 12 and 13.)

As noted in the paper, setting all of the transverse local qubit magnetic fields, B_i^x, and B_i^y values to zero in eq 1 block-diagonalizes eq A2 and may be recursively written as

$$\mathbf{H_N} = \begin{bmatrix} \mathbf{H_{N-1}^{D1}} + B_N^z \mathbf{I}_{2^{N-2}} + \mathbf{J}_{z,N}^1 & \mathbf{J}_{xy,N}^1 & \mathbf{0} & \mathbf{0} \\ \mathbf{J}_{xy,N}^{1\,T} & \mathbf{H_{N-1}^{D2}} - B_N^z \mathbf{I}_{2^{N-2}} + \mathbf{J}_{z,N}^1 & \mathbf{0} & \mathbf{0} \\ \mathbf{0} & \mathbf{0} & \mathbf{H_{N-1}^{D2}} + B_N^z \mathbf{I}_{2^{N-2}} + \mathbf{J}_{z,N}^2 & \mathbf{J}_{xxN}^2 \\ \mathbf{0} & \mathbf{0} & \mathbf{J}_{xy,N}^{2\,T} & \mathbf{H_{N-1}^{D1}} - B_N^z \mathbf{I}_{2^{N-2}} + \mathbf{J}_{z,N}^2 \end{bmatrix} \tag{A3}$$

At this stage, it is critical to realize that the two blocks in the equation above are completely decoupled and basis vector components that undergo unitary evolution due to the top block are never influenced by elements from the bottom block and vice versa. This is explicitly elaborated in Figure 11 for the case of two and three qubits. This presents us with an additional degree of flexibility for our quantum simulation. We exercise this flexibility here and map separately the top and bottom blocks of the equation above, to two different N-qubit ion trap systems controlled by parameters $\{B_i^z\, J_{ij}^\gamma\}$ and $\{\tilde{B}_i^z\, \tilde{J}_{ij}^\gamma\}$, respectively. It is important to note here that while the underlying structure of each block in the Ising Hamiltonian matrix remains the same, two different sets of ion-trap control parameters are used to simulate the top and bottom blocks, respectively, thus providing greater flexibility in simulating real systems. We, therefore, introduce a subtle change in denoting the corresponding Ising model Hamiltonian as $\mathcal{H}_\mathbf{N}$ and allow the diagonal blocks to be independently determined in the following manner

https://doi.org/10.1021/acs.jctc.1c00688
J. Chem. Theory Comput. 2021, 17, 6713−6732

$$\mathcal{H}_N = \begin{bmatrix} \mathbf{H}_N^{D1} & \mathbf{0} \\ \mathbf{0} & \tilde{\mathbf{H}}_N^{D2} \end{bmatrix} = \begin{bmatrix} \mathbf{H}_{N-1}^{D1} + B_N^z \mathbf{I}_{2^{N-2}} + \mathbf{J}_{z,N}^1 & \mathbf{J}_{xy,N}^1 & \mathbf{0} & \mathbf{0} \\ \mathbf{J}_{xy,N}^{1^T} & \mathbf{H}_{N-1}^{D2} - B_N^z \mathbf{I}_{2^{N-2}} + \mathbf{J}_{z,N}^1 & \mathbf{0} & \mathbf{0} \\ \mathbf{0} & \mathbf{0} & \tilde{\mathbf{H}}_{N-1}^{D2} + \tilde{B}_N^z \mathbf{I}_{2^{N-2}} + \tilde{\mathbf{J}}_{z,N}^2 & \tilde{\mathbf{J}}_{xy,N}^2 \\ \mathbf{0} & \mathbf{0} & \tilde{\mathbf{J}}_{xy,N}^{2^T} & \tilde{\mathbf{H}}_{N-1}^{D1} - \tilde{B}_N^z \mathbf{I}_{2^{N-2}} + \tilde{\mathbf{J}}_{z,N}^2 \end{bmatrix} \tag{A4}$$

where the top block is controlled by parameters $\{B_i^z; J_{ij}^\gamma\}$ and the bottom block is controlled by a different set of ion-trap parameters $\{\tilde{B}_i^z\ \tilde{J}_{ij}^\gamma\}$. The molecular Hamiltonian is mapped to the above form of the Ising model Hamiltonian matrix.

We now illustrate the above form of Ising Hamiltonian for the two- and three-qubit systems. But we note that the aforementioned basis set partitioning and Hamiltonian structure is completely general and applies to all cases. Explicitly written, for the case of two qubits, eq A4 takes the form

$$\mathcal{H}_2 = \begin{bmatrix} B_1^z + B_2^z + J_{12}^z & J_{12}^x - J_{12}^y & 0 & 0 \\ J_{12}^x - J_{12}^y & -B_1^z - B_2^z + J_{12}^z & 0 & 0 \\ 0 & 0 & \tilde{B}_2^z - \tilde{B}_1^z - \tilde{J}_{12}^z & \tilde{J}_{12}^x + \tilde{J}_{12}^y \\ 0 & 0 & \tilde{J}_{12}^x + \tilde{J}_{12}^y & \tilde{B}_1^z - \tilde{B}_2^z - \tilde{J}_{12}^z \end{bmatrix} \tag{A5}$$

where again we have highlighted the distinction between ion-trap simulators that represent the top block, $\{B_i^z\ J_{ij}^\gamma\}$, and those that control the bottom block, $\{\tilde{B}_i^z\ \tilde{J}_{ij}^\gamma\}$. The three-qubit Hamiltonian is then recursively obtained from the two-qubit Hamiltonian as prescribed by eq A4 and may be written in compact form as follows

$$\mathcal{H}_3 = \begin{bmatrix} \mathbf{H}_2^{D1} + B_3^z \mathbf{I}_2 + \mathbf{J}_{z,3}^1 & \mathbf{J}_{xy,3}^1 & \mathbf{0} & \mathbf{0} \\ \mathbf{J}_{xy,3}^{1^T} & \mathbf{H}_2^{D2} - B_3^z \mathbf{I}_2 + \mathbf{J}_{z,3}^1 & \mathbf{0} & \mathbf{0} \\ \mathbf{0} & \mathbf{0} & \tilde{\mathbf{H}}_2^{D2} + \tilde{B}_3^z \mathbf{I}_2 + \tilde{\mathbf{J}}_{z,3}^2 & \tilde{\mathbf{J}}_{xy,3}^2 \\ \mathbf{0} & \mathbf{0} & \tilde{\mathbf{J}}_{xy,3}^{2^T} & \tilde{\mathbf{H}}_2^{D1} - \tilde{B}_3^z \mathbf{I}_2 + \tilde{\mathbf{J}}_{z,3}^2 \end{bmatrix} \tag{A6}$$

Here, $\mathbf{H}_2^{D1}$ and $\mathbf{H}_2^{D2}$, as defined for the general case in eq A4, refer to the top and bottom diagonal blocks of the two-qubit Ising Hamiltonian (eq A5) simulated using the ion-trap parameters $\{B_i^z\ J_{ij}^\gamma\}$ while $\tilde{\mathbf{H}}_2^{D1}$ and $\tilde{\mathbf{H}}_2^{D2}$ refer to the top and bottom blocks of the two-qubit Ising Hamiltonian (eq A5) controlled by $\{\tilde{B}_i^z\ \tilde{J}_{ij}^\gamma\}$. While most of $\mathbf{H}_2^{D1}$ and $\mathbf{H}_2^{D2}$ is preserved and appear as diagonal blocks of the two-qubit Hamiltonian, the Nth qubit on-site term B_3^z and intersite coupling terms with all $N-1$ qubits J_{13}^z, J_{23}^z with appropriate phases are added to each diagonal element. The quantities $\mathbf{J}_{xy,3}^1$ and $\mathbf{J}_{xy,3}^2$ in the top block and $\tilde{\mathbf{J}}_{xy,3}^1$ and $\tilde{\mathbf{J}}_{xy,3}^2$ in the bottom block capture the interaction of qubits 1 and 2 with qubit 3 in the form of the intersite coupling terms for the two ion traps, respectively. Explicitly, the three-qubit system Hamiltonian becomes

$$\mathcal{H}_3 = \mathbf{H}_3^{D1} \oplus \tilde{\mathbf{H}}_3^{D2} \tag{A7a}$$

where, for compactness, we have written the ion-trap Hamiltonian as a direct sum of

$$\mathbf{H}_3^{D1} = \begin{bmatrix} B_1^z + B_2^z + B_3^z + J_{12}^z + J_{13}^z + J_{23}^z & J_{12}^x - J_{12}^y & J_{13}^x - J_{13}^y & J_{23}^x - J_{23}^y \\ J_{12}^x - J_{12}^y & B_3^z - B_2^z - B_1^z + J_{12}^z - J_{13}^z - J_{23}^z & J_{23}^x + J_{23}^y & J_{13}^x + J_{13}^y \\ J_{13}^x - J_{13}^y & J_{23}^x + J_{23}^y & B_2^z - B_1^z - B_3^z - J_{12}^z + J_{13}^z - J_{23}^z & J_{12}^x + J_{12}^y \\ J_{23}^x - J_{23}^y & J_{13}^x + J_{13}^y & J_{12}^x + J_{12}^y & B_1^z - B_2^z - B_3^z - J_{12}^z - J_{13}^z + J_{23}^z \end{bmatrix} \tag{A7b}$$

https://doi.org/10.1021/acs.jctc.1c00688
J. Chem. Theory Comput. 2021, 17, 6713−6732

$$\tilde{\mathbf{H}}_3^{\mathbf{D2}} = \begin{bmatrix} \tilde{B}_2^z - \tilde{B}_1^z + \tilde{B}_3^z - \tilde{J}_{12}^z - \tilde{J}_{13}^z + \tilde{J}_{23}^z & \tilde{J}_{12}^x + \tilde{J}_{12}^y & \tilde{J}_{13}^x + \tilde{J}_{13}^y & \tilde{J}_{23}^x - \tilde{J}_{23}^y \\ \tilde{J}_{12}^x + \tilde{J}_{12}^y & \tilde{B}_1^z - \tilde{B}_2^z + \tilde{B}_3^z - \tilde{J}_{12}^z + \tilde{J}_{13}^z - \tilde{J}_{23}^z & \tilde{J}_{23}^x + \tilde{J}_{23}^y & \tilde{J}_{13}^x - \tilde{J}_{13}^y \\ \tilde{J}_{13}^x + \tilde{J}_{13}^y & \tilde{J}_{23}^x + \tilde{J}_{23}^y & \tilde{B}_1^z + \tilde{B}_2^z - \tilde{B}_3^z + \tilde{J}_{12}^z - \tilde{J}_{13}^z - \tilde{J}_{23}^z & \tilde{J}_{12}^x - \tilde{J}_{12}^y \\ \tilde{J}_{23}^x - \tilde{J}_{23}^y & \tilde{J}_{13}^x - \tilde{J}_{13}^y & \tilde{J}_{12}^x - \tilde{J}_{12}^y & -\tilde{B}_1^z - \tilde{B}_2^z - \tilde{B}_3^z + \tilde{J}_{12}^z + \tilde{J}_{13}^z + \tilde{J}_{23}^z \end{bmatrix} \tag{A7c}$$

We further clarify that the top block, $\mathbf{H}_3^{\mathbf{D1}}$, is controlled by parameters $\{B_i^z\ J_{ij}^\gamma\}$, whereas the bottom block, $\tilde{\mathbf{H}}_3^{\mathbf{D1}}$, is controlled by $\{\tilde{B}_i^z\ \tilde{J}_{ij}^\gamma\}$.

APPENDIX B: OBTAINING THE ION-TRAP CONTROL PARAMETERS $\{B_i^z; J_{ij}^z\}$ FROM EQUATIONS 12 AND 13

The goal of eqs 12 and 13 is to compute the values for $\{B_i^z; J_{ij}^z\}$, given the values on the left side of eqs 12 and 13. It must first be noted that both equations are a linear set of equations, but the number of free parameters available on the right side, that is, the number of ion-trap control variables within the set $\{B_i^z; J_{ij}^z\}$, is $\{N + N(N-1)/2\}$ or $\{N(N+1)/2\}$. (In Appendix C, the number of parameters that control the ion-trap is analyzed.) On the contrary, given that the two blocks of the molecular Hamiltonian are to be propagated independently, as outlined in Appendix A, eq A4, and also in Section IV, the number of free parameters on the left sides of eqs 12 and 13 are $\{2^{N-1} - 1\} = \frac{n-1}{2}$. This quantity is obtained by realizing that each block contains 2^{N-1} diagonal elements that arise from the Givens transform of the potential energy surface and of the nuclear kinetic energy, as seen from eqs 12 and 13. But the dynamics is invariant to any shift to the potential energy surface, and thus, eliminating the average value of the diagonal elements of the molecular Hamiltonian yields a reduction of the number of free parameters in the diagonal elements of the molecular Hamiltonian leading to the quantity $\frac{n-1}{2}$.

Thus, in general, the number of ion-trap control parameters $\{B_i^z; J_{ij}^z\}$, in eqs 12 and 13, is not always equal to the number of independent control variables that arise from the molecular Hamiltonian. In this section, we present the best case solution to the set $\{B_i^z; J_{ij}^z\}$ for an arbitrary N, given the diagonal elements of the Givens-transformed molecular Hamiltonian. Furthermore, we are also in a position to provide error bounds for the case of an arbitrary number of qubits as we do later in this section.

To appropriately invert eqs 12 and 13 and to determine a suitable set of $\{B_i^z; J_{ij}^z\}$ values, we first rewrite these equations to expose the fact that the ion-trap control parameters $\{B_i^z; J_{ij}^z\}$ are specific Hadamard transforms of $\langle\tilde{x}|\,\mathcal{H}^{Mol}|\tilde{x}\rangle$ as stated in eq 14. To achieve this, we treat all parameters in $\{B_i^z; J_{ij}^z\}$ on an equal footing and assign these to a new set of variables $\{B_i^z; J_{ij}^z\} \equiv D_l^z$, where the index "$l$" runs over all integer values less than or equal to

$$BJ_{\min}^z \equiv \min\left(N(N+1)/2, \frac{n-1}{2}\right) \tag{B1}$$

as is clear from the above discussion. We, thus, write the mapping expression for the diagonal elements, from eqs 12 and 13 as

$$[K(x_i, x_i) - K(x_i, x_{n-i})] + \frac{1}{2}[V(x_i) + V(x_{n-i})] = \sum_{j=1}^{N}(-1)^{\tilde{\lambda}_j} B_j^z + \sum_{j=1}^{N-1}\sum_{k>j}^{N}(-1)^{\tilde{\lambda}_j \oplus \tilde{\lambda}_k} J_{jk}^z \equiv \sum_{l=1}^{BJ_{\min}^z} \mathbf{T}_{\tilde{\lambda},l} D_l^z$$

$$\text{for } i < n/2 \tag{B2}$$

and

$$[K(x_i, x_i) + K(x_i, x_{n-i})] + \frac{1}{2}[V(x_i) + V(x_{n-i})] = \sum_{j=1}^{N}(-1)^{\tilde{\lambda}_j} B_j^z + \sum_{j=1}^{N-1}\sum_{k>j}^{N}(-1)^{\tilde{\lambda}_j \oplus \tilde{\lambda}_k} J_{jk}^z \equiv \sum_{l=1}^{BJ_{\min}^z} \mathbf{T}_{\tilde{\lambda},l} D_l^z$$

$$\text{for } i > n/2 \tag{B3}$$

where $\{\tilde{\lambda}\}$ corresponds to either of the two sets of permuted computational basis states (see Figure 3) that independently span $\{\mathbf{S}^{+^{2n}}|\downarrow\downarrow\cdots\rangle\}$ or $\{\mathbf{S}^{+^{2n-1}}|\downarrow\downarrow\cdots\rangle\}$ and $\mathbf{T}_{\tilde{\lambda},l}$ represents a coefficient matrix for the phase preceding the corresponding D_l^z in the equations above. The upper limit, $BJ_{\min}^z$, to the summation in eqs B2 and B3 thus denotes the maximum number of independent parameters in $\{B_j^z; J_{jk}^z\}$ that will be used to encode the diagonal part of $\tilde{\mathcal{H}}^{\mathrm{Mol}}$ for a given number of qubits. Thus, the diagonal elements of the transformed Ising Hamiltonian $\langle\tilde{\lambda}|\,\mathcal{H}_{\mathrm{IT}}|\tilde{\lambda}\rangle$ encode both the Givens-transformed Born−Oppenheimer potential energy surface, $V(x)$, and the nuclear kinetic energy that appear due to the block diagonalization process, needed to make the two Hamiltonians have the same structure (see eqs 7, 12, and 13). The columns of the transformation matrix on the right side of eqs B2 and B3, with elements, $\mathbf{T}_{\tilde{\lambda},l} = \pm 1$, resemble a subset of columns that span an $N-1$-dimensional Hadamard matrix, which is an $(N-1)$th-order tensor product of the standard 2×2 (or one-qubit) Hadamard transform. Thus, the columns of $\mathbf{T}$ in eqs B2 and B3 form an orthonormal set and thus the $\{B_j^z; J_{jk}^z\}$ values represent a rotation of the elements in $\langle\tilde{x}|\,\mathcal{H}^{\mathrm{Mol}}|\tilde{x}\rangle$.

$$D_l^z = \frac{1}{2^{N-1}} \sum_{\{\tilde{\lambda}\}} \mathbf{T}_{l,\tilde{\lambda}} \langle\tilde{\lambda}|\,\mathcal{H}_{\mathrm{IT}}|\tilde{\lambda}\rangle \tag{B4}$$

Owing to the equivalence of $\langle\tilde{x}|\,\mathcal{H}^{\mathrm{Mol}}|\tilde{x}\rangle$ and $\langle\tilde{\lambda}|\,\mathcal{H}_{\mathrm{IT}}|\tilde{\lambda}\rangle$, as seen in eqs 9 and B4, we use the precomputed diagonal elements of the unitary-transformed molecular Hamiltonian in eq B4 to obtain the on-site parameters of the ion trap. As per

https://doi.org/10.1021/acs.jctc.1c00688
J. Chem. Theory Comput. 2021, 17, 6713−6732

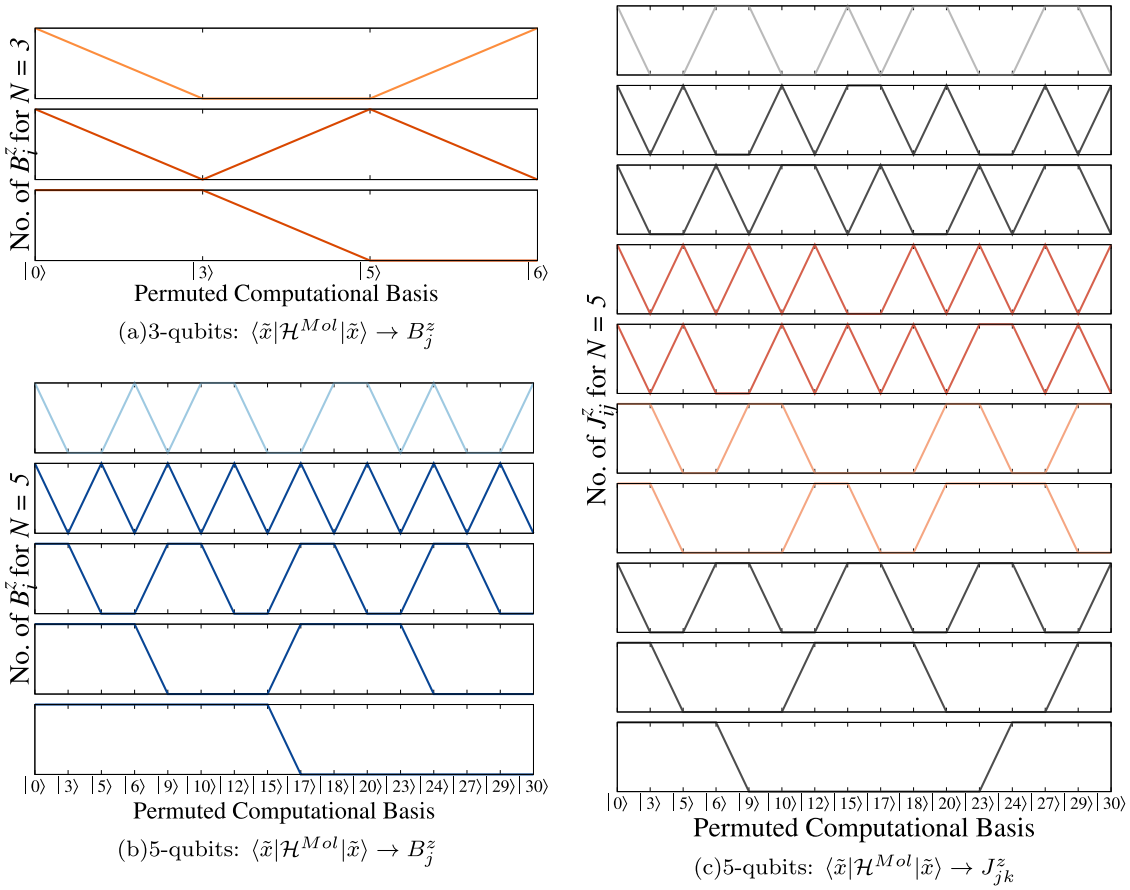

Figure 12. Transformation from $\langle\tilde{x}|\,\mathcal{H}^{\mathrm{Mol}}|\tilde{x}\rangle$ to the B^z-values for three qubits (a) and B^z (b) and J^z-values (c) for five qubits. This inverse matrix picks out the appropriate columns from the 2^{N-1}-dimensional Hadamard transformation matrix. See eqs 11 and B5. The B^z transformations (a, b) arise from two basic vectors (top and bottom). The vector in the bottom panel is scaled in frequency to create the other vectors. This aspect is shown using two different color shades. Similarly, J^z transformations (c) arise from five basic transformations arranged with different color shades in panels 1-3, 4-5, 6-7, 8-9, and 10.

eq 11, $\langle\tilde{\lambda}|\,\mathcal{H}_{\mathrm{IT}}|\tilde{\lambda}\rangle$ may be replaced by $\langle\tilde{x}|\,\mathcal{H}^{\mathrm{Mol}}|\tilde{x}\rangle$ in eq B4 leading to

$$D_l^z = \frac{1}{2^{N-1}} \sum_{\{\tilde{x}\}\Leftrightarrow\{\tilde{\lambda}\}} \mathbf{T}_{l,\tilde{\lambda}} \langle\tilde{x}|\,\mathcal{H}^{\mathrm{Mol}}|\tilde{x}\rangle \tag{B5}$$

where we tersely assume the summation over $\{\tilde{\lambda}\}$ to also correspond to the summation over $\{\tilde{x}\}$ as allowed by the correspondence in eq 10. Furthermore, since the N-qubit-Hadamard transform is unitary, we have simply transposed the elements of the transformation matrix, $\mathbf{T}$, in writing eq B5. For example, for the three-qubit case studied here, the tensor product of two Hadamard matrices yields

$$H_2 = \frac{1}{2}\begin{pmatrix} 1 & 1 & 1 & 1 \\ 1 & -1 & 1 & -1 \\ 1 & 1 & -1 & -1 \\ 1 & -1 & -1 & 1 \end{pmatrix} \tag{B6}$$

Hence, the transformation matrix in eq B5 is obtained from eq B6, by removing the zero-frequency component (first row) leading to

$$[\mathbf{T}]^T = \begin{pmatrix} 1 & -1 & -1 & 1 \\ 1 & -1 & 1 & -1 \\ 1 & 1 & -1 & -1 \end{pmatrix} \tag{B7}$$

The first row of eq B6 is the average of the diagonal elements of the molecular Hamiltonian and, as noted at the top of this section, the diagonal elements, $\langle\tilde{x}|\,\mathcal{H}^{\mathrm{Mol}}|\tilde{x}\rangle$, are shifted so that this average value is zero. This uniform shift of the diagonal elements results in a constant shift between the eigenvalues of the molecular Hamiltonian and the Ising Hamiltonian, which results in no change to the dynamics, as is clear from Figures 8−10.

The transformation matrix in eq B5, that is, $\mathbf{T}^T$, is also illustrated in Figure 12b,c for the 2^4-dimensional sub-blocks of a five-qubit Ising and for the 2^2-dimensional sub-blocks of a three-qubit Ising Hamiltonian in Figure 12a. The dimension $2^{N-1} \times \frac{N(N+1)}{2}$ of the $\mathbf{T}$ matrix is apparent from this figure. The latter dimension of the $\mathbf{T}$ matrix that depends on the number of independent D_l^z values is at most $\frac{N(N+1)}{2}$ (or $BJ_{\min}^z$) and is found to be 3 for the three-qubit system and 15 for the five-qubit system. While the figure is only presented for three-qubit and five-qubit systems, the transformation is completely general.

https://doi.org/10.1021/acs.jctc.1c00688
J. Chem. Theory Comput. 2021, 17, 6713−6732

ERROR BOUNDS ON MAPPING $\langle\tilde{x}|\mathcal{H}^{\mathrm{Mol}}|\tilde{x}\rangle \leftrightarrow \langle\tilde{\lambda}|\mathcal{H}_{\mathrm{IT}}|\tilde{\lambda}\rangle$ FOR A LARGER NUMBER OF QUBITS

Arising from the above discussion, the error, ϵ, associated with such a partial Hadamard transform of the diagonal elements of the molecular Hamiltonian, can be obtained from the orthogonal complements of the transformation matrix in the corresponding Hadamard matrix. This can be expressed in a closed form as

$$\epsilon = \frac{1}{2^{N-1}}\sqrt{([\tilde{\mathcal{H}}^{\mathrm{Mol}}_{\mathrm{Diag}}]^T \mathbf{P}^{\mathbf{T}_\perp}[\tilde{\mathcal{H}}^{\mathrm{Mol}}_{\mathrm{Diag}}]} \tag{B8}$$

where $\tilde{\mathcal{H}}^{\mathrm{Mol}}_{\mathrm{Diag}}$ contains the diagonal elements of $\tilde{\mathcal{H}}^{\mathrm{Mol}}$, that is, $\langle\tilde{x}|\mathcal{H}^{\mathrm{Mol}}|\tilde{x}\rangle$, in the equations above and $\mathbf{P}^{\mathbf{T}_\perp}$ is a projector on to the orthogonal complement of transformation matrix $\mathbf{T}$ (depicted in Figure 12 for three and five qubits) as obtained from the Hadamard matrix.

$$\begin{aligned}\mathbf{P}^{\mathbf{T}_\perp} &\equiv 2^{N-1}H^{\otimes(N-1)}H^{\otimes(N-1)^T} - \mathbf{T}\mathbf{T}^T \\ &= 2^{N-1}\mathbf{I}_{2^{(N-1)}} - \mathbf{T}\mathbf{T}^T\end{aligned} \tag{B9}$$

where the quantity $H^{\otimes(N-1)}$ is the $(N-1)$th-order tensor product of the standard 2×2 (or one-qubit) Hadamard transform. Thus, cases where the diagonal part of the molecular Hamiltonian is exactly captured within the subspace represented by eq B5 may be exactly modeled using the ion-trap simulator/computer. In all of these cases, the orthogonal complement in eq B8 is identically zero. In the general case, the problem becomes that of suitably representing the diagonal elements of the molecular Hamiltonian within the subspace of Hadamard transforms represented by $\mathbf{T}^T$.

APPENDIX C: NUMBER OF DEGREES OF CONTROL IN THE ISING HAMILTONIAN, EQUATION 1

For a given number of qubits, N, the number of ion-trap handles in eq 1 that control various sectors of the Hamiltonian matrix scale as

$$\{N + N(N-1)/2\} + \{N(N-1)\} + \{2N\} \rightarrow \mathcal{O}(N^2) \tag{C1}$$

Here, the first quantity, $\{N + N(N-1)/2\}$, refers to the parameters, $\{B_i^z; J_{ij}^z\}$, that control the diagonal elements of the matrix (actively discussed in Appendix B), the second quantity on the left, $\{N(N-1)\}$, refers to the parameters, $\{J_{ij}^x \pm J_{ij}^y\}$, that control the coupling between the basis vectors inside each block, and $\{2N\}$ refers to the parameters, $\{B_i^x \pm B_i^y\}$, that control the coupling across the sets of basis vectors created using the odd and even raising operators described above. This characterization not only elucidates the degrees of freedom of the Ising model Hamiltonian in eq 1 but also provides the sectored availability of these control parameters.

At this stage, there are two cases that become interesting insofar as mapping to realistic systems is concerned. In the first case, the structure of the Ising Hamiltonian is used as is, including the $\{B_i^x \pm B_i^y\}$ terms, and the number of degrees of freedom is as given above and must match the same for the problem at hand to produce an *exact* map. For the second case, if the $\{B_i^x \pm B_i^y\}$ handles are eliminated, the system reduces to two separate blocks that may be propagated independently, perhaps even on two different sets of ion-trap architectures arranged in parallel, or Trotterized on one single ion-trap architecture. It is this second case that we consider in this paper as it allows the ability to have different Ising model parameters for the two diagonal blocks, and in this case, the number of ion-trap handles become

$$2\{N + N(N-1)/2 + N(N-1)\} \tag{C2}$$

which is, in fact, greater than the number of Ising model handles available in an $(N-1)$-qubit system when $N < 17$. The above discussion also implies that for Hamiltonians containing 2^N independent terms, only approximate computation is possible. In this sense, the current paper takes a first step toward providing the necessary accuracy bounds in Appendix B.

APPENDIX D: THE "DISTRIBUTED APPROXIMATING FUNCTIONAL" (DAF) REPRESENTATION FOR THE KINETIC ENERGY OPERATOR (EQUATION 3)

The DAF approach has been well reviewed in the literature.[68,69] But given the significance of the banded Toeplitz form toward the mapping algorithm, where as seen in eq 8, the contributions to the off-diagonal blocks from the kinetic energy go to zero due to the banded Toeplitz representation, we present a brief summary of the DAF representation here. The starting point is to expand the wavepacket at time $t = 0$ using a local set of symmetric fitting functions, $a(x - x_i)$, such that

$$\chi(x;\, t=0) = \sum_i \Delta x_i a(x - x_i)\chi(x_i;\, t=0) \tag{D1}$$

where Δx_i is the grid spacing (not in general uniform). The functions $a(x - x_i)$ are local fitting functions, the choice for which may, in general, depend upon the point x_i. One of the most common directions at this point is to assume that $a(x - x_i) \equiv \delta(x - x_i) \equiv \langle x|x_i\rangle$ is a suitable approximation to the Dirac delta function. Subsequent resolution of the identity in terms of some complete set of basis functions leads to a representation of the wavepacket in that basis. The DAF approximation differs from these approaches by assuming that a suitable local representation[69,84] can be directly constructed for $a(x - x_i)$, that is

$$\begin{aligned}a(x - x_i) &\equiv a_N(x - x_i;\, \sigma) \\ &= \sum_n^N b_n H_n\left(\frac{x - x_i}{\sqrt{2}\,\sigma}\right)\exp\left[-\frac{(x - x_i)^2}{2\sigma^2}\right]\end{aligned} \tag{D2}$$

where $H_n(x)$ are the Hermite polynomials generated from Gaussians according to

$$H_n(y)\exp[-y] = (-1)^n \frac{\mathrm{d}^n}{\mathrm{d}y^n}\exp[-y] \tag{D3}$$

Note that eq D2 is different from the expression obtained using a standard basis set approximation for $a(x - x_i)$, wherein the appropriate expression would be

https://doi.org/10.1021/acs.jctc.1c00688
J. Chem. Theory Comput. 2021, 17, 6713−6732

$$a(x - x_i) \equiv \delta(x - x_i) = \sum_n c_n \{ \exp[-x^2/2] H_n(x) \} \times \{ \exp[-x_i^2/2] H_n(x_i) \} \quad \text{(D4)}$$

with $c_n = (\sqrt{\pi} 2^n n!)^{-1}$. Note that eq D4 is separable in x and x_i, whereas eq D2 only depends on $(x - x_i)$. The local spectral[85] form in eq D2 has many computational advantages not the least of which is the fact that eq D2 yields a banded Toeplitz matrix at any level of approximation. The choice of Hermite functions here is by no means a requirement; it is however a convenient choice. Using the orthogonality of the Hermite functions and the fact that $a(x - x_i)$ must be symmetric with respect to interchange of x and x_i (since it approximates the Dirac delta function), one obtains

$$b_{2n+1} = 0$$
$$b_{2n} = \frac{1}{\sigma\sqrt{2\pi}} \left(-\frac{1}{4}\right)^n \frac{1}{n!} \quad \text{(D5)}$$

where we have used the identity[86]

$$\int dy \exp[-y^2] H_n(y) H_m(y) \equiv \delta_{n,m} 2^m m! \sqrt{\pi} \quad \text{(D6)}$$

thus resulting in eq 3. The variables M and σ determine the accuracy and width (or computational efficiency), respectively, of the DAF. It has been shown[69,87,88] that these parameters are not independent, and for a given value of M, there exists a σ that provides optimal accuracy for the propagation. The accuracy of this method in conjunction with *ab initio* dynamics has been benchmarked in ref 88. For an approximation controlled by choice of parameters M and σ, eq 3 only depends on the quantity $(x - x')$, that is, distance between points in the coordinate representation, and goes to zero as this quantity becomes numerically large due to the Gaussian prefactor. This yields a banded matrix approximation to eq 3, for any M and σ. Furthermore, on account of its dependence on $(x - x')$, a matrix representation of eq 3 has the property that all diagonal elements of this matrix are equal; similarly, all n-th super (and sub)diagonal elements are the same. Such a matrix is called a Toeplitz matrix. The dependence on $(x - x')$ also implies a translational symmetry reminiscent of wavelet theories.[89−92]

We finally note that the DAF approach differs from other approaches that use Hermite functions to represent the wavepacket[93,94] based on Heller's Gaussian wavepacket formalism.[95] Within these formalisms,[93,94] a locally harmonic approximation to the potential[95] allows the reduction of the time-dependent Schrödinger equation to classical-like equations to propagate the width and center of the Gaussian wavepackets. In our case, no assumption is made on the nature of the potential.

AUTHOR INFORMATION

Corresponding Authors

Srinivasan S. Iyengar − *Department of Chemistry, and the Indiana University Quantum Science and Engineering Center (IU-QSEC), Indiana University, Bloomington, Indiana 47405, United States;* orcid.org/0000-0001-6526-2907; Email: iyengar@indiana.edu

Philip Richerme − *Department of Physics and the Indiana University Quantum Science and Engineering Center (IU-QSEC), Indiana University, Bloomington, Indiana 47405, United States;* Email: richerme@indiana.edu

Authors

Debadrita Saha − *Department of Chemistry, and the Indiana University Quantum Science and Engineering Center (IU-QSEC), Indiana University, Bloomington, Indiana 47405, United States*

Jeremy M. Smith − *Department of Chemistry, Indiana University, Bloomington, Indiana 47405, United States;* orcid.org/0000-0002-3206-4725

Amr Sabry − *Department of Computer Science, School of Informatics, Computing, and Engineering, and the Indiana University Quantum Science and Engineering Center (IU-QSEC), Indiana University, Bloomington, Indiana 47405, United States*

Complete contact information is available at: https://pubs.acs.org/10.1021/acs.jctc.1c00688

Notes

The authors declare no competing financial interest.

ACKNOWLEDGMENTS

This research was supported by the National Science Foundation grant OMA-1936353 to S.S.I., P.R., J.M.S., and A.S. The authors are grateful to Dr. Miguel Ángel López Ruiz for valuable comments.

REFERENCES

(1) Weinberg, D. R.; Gagliardi, C. J.; Hull, J. F.; Fecenko Murphy, C.; Kent, C. A.; Westlake, B. C.; Paul, A.; Ess, D. H.; McCafferty, D. G.; Meyer, T. J. Proton-Coupled Electron Transfer. *Chem. Rev.* **2012**, *112*, 4016−4093.

(2) Nagel, Z.; Klinman, J. Tunneling and Dynamics in Enzymatic Hydride Transfer. *Chem. Rev.* **2006**, *106*, 3095.

(3) Soudackov, A. V.; Hammes-Schiffer, S. Probing Nonadiabaticity in the Proton-Coupled Electron Transfer Reaction Catalyzed by Soybean Lipoxygenase. *J. Phys. Chem. Lett.* **2014**, *5*, 3274.

(4) *Hydrogen-Transfer Reactions*; Hynes, J. T.; Klinman, J. P.; Limbach, H.-H.; Schowen, R. L., Eds.; Wiley-VCH: Weinheim, Germany, 2007.

(5) Cukier, R. I.; Nocera, D. G. Proton-coupled electron transfer. *Annu. Rev. Phys. Chem.* **1998**, *49*, 337−369.

(6) Mayer, J. M. Proton-coupled electron transfer: A Reaction Chemistas View. *Annu. Rev. Phys. Chem.* **2004**, *55*, 363−390.

(7) Hammes-Schiffer, S. Catalysts by Design: The Power of Theory. *Acc. Chem. Res.* **2017**, *50*, 561−566.

(8) Raghavachari, K.; Trucks, G. W.; Pople, J. A.; Head-Gordon, M. A fifth-order perturbation comparison of electron correlation theories. *Chem. Phys. Lett.* **1989**, *157*, 479−483.

(9) O'Malley, P. J. J.; Babbush, R.; Kivlichan, I. D.; Romero, J.; McClean, J. R.; Barends, R.; Kelly, J.; Roushan, P.; Tranter, A.; Ding, N.; Campbell, B.; Chen, Y.; Chen, Z.; Chiaro, B.; Dunsworth, A.; Fowler, A. G.; Jeffrey, E.; Lucero, E.; Megrant, A.; Mutus, J. Y.; Neeley, M.; Neill, C.; Quintana, C.; Sank, D.; Vainsencher, A.; Wenner, J.; White, T. C.; Coveney, P. V.; Love, P. J.; Neven, H.; Aspuru-Guzik, A.; Martinis, J. M. Scalable quantum simulation of molecular energies. *Phys. Rev. X* **2016**, *6*, No. 031007.

(10) Kandala, A.; Mezzacapo, A.; Temme, K.; Takita, M.; Brink, M.; Chow, J. M.; Gambetta, J. M. Hardware-efficient variational quantum eigensolver for small molecules and quantum magnets. *Nature* **2017**, *549*, 242.

(11) Xia, R.; Kais, S. Quantum machine learning for electronic structure calculations. *Nat. Commun.* **2018**, *9*, No. 4195.

(12) Gorman, D. J.; Hemmerling, B.; Megidish, E.; Moeller, S. A.; Schindler, P.; Sarovar, M.; Haeffner, H. Engineering Vibrationally Assisted Energy Transfer in a Trapped-Ion Quantum Simulator. *Phys. Rev. X* **2018**, *8*, No. 011038.
(13) Nam, Y.; Chen, J.-S.; Pisenti, N. C.; Wright, K.; Delaney, C.; Maslov, D.; Brown, K. R.; Allen, S.; Amini, J. M.; Apisdorf, J.; Beck, K. M.; Blinov, A.; Chaplin, V.; Chmielewski, M.; Collins, C.; Debnath, S.; Hudek, K. M.; Ducore, A. M.; Keesan, M.; Kreikemeier, S. M.; Mizrahi, J.; Solomon, P.; Williams, M.; Wong-Campos, J. D.; Moehring, D.; Monroe, C.; Kim, J. Ground-state energy estimation of the water molecule on a trapped ion quantum computer. *npj Quantum Inf.* **2020**, *6*, No. 33.
(14) Wang, B.-X.; Tao, M.-J.; Ai, Q.; Xin, T.; Lambert, N.; Ruan, D.; Cheng, Y.-C.; Nori, F.; Deng, F.-G.; Long, G.-L. Efficient quantum simulation of photosynthetic light harvesting. *npj Quantum Inf.* **2018**, *4*, No. 52.
(15) Chin, A. W.; Mangaud, E.; Atabek, O.; Desouter-Lecomte, M. Coherent quantum dynamics launched by incoherent relaxation in a quantum circuit simulator of a light-harvesting complex. *Phys. Rev. A* **2018**, *97*, No. 063823.
(16) Potočnik, A.; Bargerbos, A.; Schroder, F. A. Y. N.; Khan, S. A.; Collodo, M. C.; Gasparinetti, S.; Salathe, Y.; Creatore, C.; Eichler, C.; Tureci, H. E.; Chin, A. W.; Wallraff, A. Studying light-harvesting models with superconducting circuits. *Nat. Commun.* **2018**, *9*, No. 904.
(17) Peruzzo, A.; McClean, J.; Shadbolt, P.; Yung, M.-H.; Zhou, X.-Q.; Love, P. J.; Aspuru-Guzik, A.; O'brien, J. L. A variational eigenvalue solver on a photonic quantum processor. *Nat. Commun.* **2014**, *5*, No. 4213.
(18) Grimsley, H. R.; Economou, S. E.; Barnes, E.; Mayhall, N. J. An adaptive variational algorithm for exact molecular simulations on a quantum computer. *Nat. Commun.* **2019**, *10*, No. 3007.
(19) Arute, F.; Arya, K.; Babbush, R.; Bacon, D.; Bardin, J. C.; Barends, R.; Boixo, S.; Broughton, M.; Buckley, B. B.; Buell, D. A.; Burkett, B.; Bushnell, N.; Chen, Y.; Chen, Z.; Chiaro, B.; Collins, R.; Courtney, W.; Demura, S.; Dunsworth, A.; Farhi, E.; Fowler, A.; Foxen, B.; Gidney, C.; Giustina, M.; Graff, R.; Habegger, S.; Harrigan, M. P.; Ho, A.; Hong, S.; Huang, T.; Huggins, W. J.; Ioffe, L.; Isakov, S. V.; Jeffrey, E.; Jiang, Z.; Jones, C.; Kafri, D.; Kechedzhi, K.; Kelly, J.; Kim, S.; Klimov, P. V.; Korotkov, A.; Kostritsa, F.; Landhuis, D.; Laptev, P.; Lindmark, M.; Lucero, E.; Martin, O.; Martinis, J. M.; McClean, J. R.; McEwen, M.; Megrant, A.; Mi, X.; Mohseni, M.; Mruczkiewicz, W.; Mutus, J.; Naaman, O.; Neeley, M.; Neill, C.; Neven, H.; Niu, M. Y.; O'Brien, T. E.; Ostby, E.; Petukhov, A.; Putterman, H.; Quintana, C.; Roushan, P.; Rubin, N. C.; Sank, D.; Satzinger, K. J.; Smelyanskiy, V.; Strain, D.; Sung, K. J.; Szalay, M.; Takeshita, T. Y.; Vainsencher, A.; White, T.; Wiebe, N.; Yao, Z. J.; Yeh, P.; Zalcman, A. Hartree-Fock on a superconducting qubit quantum computer. *Science* **2020**, *369*, 1084−1089.
(20) Parrish, R. M.; Hohenstein, E. G.; McMahon, P. L.; Martinez, T. J. Quantum Computation of Electronic Transitions Using a Variational Quantum Eigensolver. *Phys. Rev. Lett.* **2019**, *122*, No. 230401.
(21) Jordan, P.; Wigner, E. Über das Paulische Äquivalenzverbot. *Z. Phys.* **1928**, *47*, 631−651.
(22) Ortiz, G.; Gubernatis, J. E.; Knill, E.; Laflamme, R. Quantum algorithms for fermionic simulations. *Phys. Rev. A* **2001**, *64*, No. 022319.
(23) Bravyi, S. B.; Kitaev, A. Y. Fermionic Quantum Computation. *Ann. Phys.* **2002**, *298*, 210−226.
(24) Iyengar, S. S.; Sumner, I.; Jakowski, J. Hydrogen Tunneling in an Enzyme Active Site: A Quantum Wavepacket Dynamical Perspective. *J. Phys. Chem. B* **2008**, *112*, 7601.
(25) Sumner, I.; Iyengar, S. S. Analysis of Hydrogen Tunneling in an Enzyme Active Site Using von Neumann Measurements. *J. Chem. Theory Comput.* **2010**, *6*, 1698.
(26) Tkachenko, N. V.; Sud, J.; Zhang, Y.; Tretiak, S.; Anisimov, P. M.; Arrasmith, A. T.; Coles, P. J.; Cincio, L.; Dub, P. A. Correlation-Informed Permutation of Qubits for Reducing Ansatz Depth in the Variational Quantum Eigensolver. *PRX Quantum2021* **2021**, *2*, 020337.
(27) Cervera-Lierta, A.; Kottmann, J. S.; Aspuru-Guzik, A. Meta-Variational Quantum Eigensolver: Learning Energy Profiles of Parameterized Hamiltonians for Quantum Simulation. *PRX Quantum2021* **2021**, *2*, 020329.
(28) Huggins, W. J.; McClean, J. R.; Rubin, N. C.; Jiang, Z.; Wiebe, N.; Whaley, K. B.; Babbush, R. Efficient and noise resilient measurements for quantum chemistry on near-term quantum computers. *npj Quantum Inf.* **2021**, *7*, No. 23.
(29) McClean, J. R.; Rubin, N. C.; Sung, K. J.; Kivlichan, I. D.; Bonet-Monroig, X.; Cao, Y.; Dai, C.; Fried, E. S.; Gidney, C.; Gimby, B.; et al. OpenFermion: the electronic structure package for quantum computers. *Quantum Sci. Technol.* **2020**, *5*, No. 034014.
(30) Motta, M.; Gujarati, T. P.; Rice, J. E.; Kumar, A.; Masteran, C.; Latone, J. A.; Lee, E.; Valeev, E. F.; Takeshita, T. Y. Quantum simulation of electronic structure with a transcorrelated Hamiltonian: improved accuracy with a smaller footprint on the quantum computer. *Phys. Chem. Chem. Phys.* **2020**, *22*, 24270−24281.
(31) Kassal, I.; Jordan, S. P.; Love, P. J.; Mohseni, M.; Aspuru-Guzik, A. Polynomial-time quantum algorithm for the simulation of chemical dynamics. *Proc. Natl. Acad. Sci. U.S.A.* **2008**, *105*, 18681−18686.
(32) MacDonell, R. J.; Dickerson, C. E.; Birch, C. J. T.; Kumar, A.; Edmunds, C. L.; Biercuk, M. J.; Hempel, C.; Kassal, I. Analog quantum simulation of chemical dynamics. *Chem. Sci.* **2020**, 9794−9805.
(33) Ollitrault, P. J.; Baiardi, A.; Reiher, M.; Tavernelli, I. Hardware efficient quantum algorithms for vibrational structure calculations. *Chem. Sci.* **2020**, *11*, 6842−6855.
(34) Sawaya, N. P.; Menke, T.; Kyaw, T. H.; Johri, S.; Aspuru-Guzik, A.; Guerreschi, G. G. Resource-efficient digital quantum simulation of d-level systems for photonic, vibrational, and spin-s Hamiltonians. *npj Quantum Inf.* **2020**, *6*, No. 49.
(35) Teplukhin, A.; Kendrick, B. K.; Babikov, D. Solving complex eigenvalue problems on a quantum annealer with applications to quantum scattering resonances. *Phys. Chem. Chem. Phys.* **2020**, *22*, 26136−26144.
(36) Jahangiri, S.; Arrazola, J. M.; Quesada, N.; Delgado, A. Quantum algorithm for simulating molecular vibrational excitations. *Phys. Chem. Chem. Phys.* **2020**, *22*, 25528−25537.
(37) Wang, C. S.; Curtis, J. C.; Lester, B. J.; Zhang, Y.; Gao, Y. Y.; Freeze, J.; Batista, V. S.; Vaccaro, P. H.; Chuang, I. L.; Frunzio, L.; Jiang, L.; Girvin, S. M.; Schoelkopf, R. J. Efficient Multiphoton Sampling of Molecular Vibronic Spectra on a Superconducting Bosonic Processor. *Phys. Rev. X* **2020**, *10*, No. 021060.
(38) Porras, D.; Cirac, J. I. Effective Quantum Spin Systems with Trapped Ions. *Phys. Rev. Lett.* **2004**, *92*, No. 207901.
(39) Richerme, P.; Gong, Z.-X.; Lee, A.; Senko, C.; Smith, J.; Foss-Feig, M.; Michalakis, S.; Gorshkov, A. V.; Monroe, C. Non-local propagation of correlations in quantum systems with long-range interactions. *Nature* **2014**, *511*, 198−201.
(40) Xia, R.; Bian, T.; Kais, S. Electronic Structure Calculations and the Ising Hamiltonian. *J. Phys. Chem. B* **2018**, *122*, 3384−3395.
(41) Bravyi, S.; Hastings, M. On Complexity of the Quantum Ising Model. *Commun. Math. Phys.* **2017**, *349*, 1−45.
(42) Copenhaver, J.; Wasserman, A.; Wehefritz-Kaufmann, B. Using quantum annealers to calculate ground state properties of molecules. *J. Chem. Phys.* **2021**, *154*, No. 034105.
(43) Barends, R.; Kelly, J.; Megrant, A.; Veitia, A.; Sank, D.; Jeffrey, E.; White, T. C.; Mutus, J.; Fowler, A. G.; Campbell, B.; Chen, Y.; Chen, Z.; Chiaro, B.; Dunsworth, A.; Neill, C.; O'Malley, P.; Roushan, P.; Vainsencher, A.; Wenner, J.; Korotkov, A. N.; Cleland, A. N.; Martinis, J. M. Superconducting quantum circuits at the surface code threshold for fault tolerance. *Nature* **2014**, *508*, 500−503.
(44) Lanyon, B. P.; Whitfield, J. D.; Gillett, G. G.; Goggin, M. E.; Almeida, M. P.; Kassal, I.; Biamonte, J. D.; Mohseni, M.; Powell, B.

https://doi.org/10.1021/acs.jctc.1c00688
J. Chem. Theory Comput. 2021, 17, 6713−6732

J.; Barbieri, M.; Aspuru-Guzik, A.; White, A. G. Towards quantum chemistry on a quantum computer. *Nat. Chem.* **2010**, *2*, 106−111.
(45) Aspuru-Guzik, A.; Walther, P. Photonic quantum simulators. *Nat. Phys.* **2012**, *8*, 285−291.
(46) Knill, E.; Laflamme, R.; Milburn, G. J. A scheme for efficient quantum computation with linear optics. *Nature* **2001**, *409*, 46−52.
(47) Pellizzari, T.; Gardiner, S. A.; Cirac, J. I.; Zoller, P. Decoherence, continuous observation, and quantum computing: A cavity QED model. *Phys. Rev. Lett.* **1995**, *75*, No. 3788.
(48) Loss, D.; DiVincenzo, D. P. Quantum computation with quantum dots. *Phys. Rev. A* **1998**, *57*, No. 120.
(49) Imamoglu, A.; Awschalom, D. D.; Burkard, G.; DiVincenzo, D. P.; Loss, D.; Sherwin, M.; Small, A. Quantum information processing using quantum dot spins and cavity QED. *Phys. Rev. Lett.* **1999**, *83*, No. 4204.
(50) Calarco, T.; Datta, A.; Fedichev, P.; Pazy, E.; Zoller, P. Spin-based all-optical quantum computation with quantum dots: Understanding and suppressing decoherence. *Phys. Rev. A* **2003**, *68*, No. 012310.
(51) Saffman, M.; Walker, T. G.; Mølmer, K. Quantum information with Rydberg atoms. *Rev. Mod. Phys.* **2010**, *82*, No. 2313.
(52) Bernien, H.; Schwartz, S.; Keesling, A.; Levine, H.; Omran, A.; Pichler, H.; Choi, S.; Zibrov, A. S.; Endres, M.; Greiner, M.; Vuletić, V.; Lukin, M. D. Probing many-body dynamics on a 51-atom quantum simulator. *Nature* **2017**, *551*, 579−584.
(53) Golub, G. H.; Van Loan, C. F. *Matrix Computations*; JHU Press, 2013; Vol. *3*.
(54) Britton, J. W.; Sawyer, B. C.; Keith, A. C.; Wang, C.-C. J.; Freericks, J. K.; Uys, H.; Biercuk, M. J.; Bollinger, J. J. Engineered two-dimensional Ising interactions in a trapped-ion quantum simulator with hundreds of spins. *Nature* **2012**, *484*, 489−492.
(55) Wang, Y.; Um, M.; Zhang, J.; An, S.; Lyu, M.; Zhang, J.-N.; Duan, L.-M.; Yum, D.; Kim, K. Single-qubit quantum memory exceeding ten-minute coherence time. *Nat. Photonics* **2017**, *11*, 646.
(56) Mølmer, K.; Sórensen, A. Multiparticle entanglement of hot trapped ions. *Phys. Rev. Lett.* **1999**, *82*, No. 1835.
(57) Noek, R.; Vrijsen, G.; Gaultney, D.; Mount, E.; Kim, T.; Maunz, P.; Kim, J. High speed, high fidelity detection of an atomic hyperfine qubit. *Opt. Lett.* **2013**, *38*, 4735−4738.
(58) Ludlow, A. D.; Boyd, M. M.; Ye, J.; Peik, E.; Schmidt, P. O. Optical atomic clocks. *Rev. Mod. Phys.* **2015**, *87*, No. 637.
(59) Blatt, R.; Roos, C. F. Quantum simulations with trapped ions. *Nat. Phys.* **2012**, *8*, 277.
(60) Islam, R.; et al. Emergence and frustration of magnetism with variable-range interactions in a quantum simulator. *Science* **2013**, *340*, 583−587.
(61) Richerme, P.; Senko, C.; Smith, J.; Lee, A.; Korenblit, S.; Monroe, C. Experimental performance of a quantum simulator: Optimizing adiabatic evolution and identifying many-body ground states. *Phys. Rev. A* **2013**, *88*, No. 012334.
(62) Senko, C.; Smith, J.; Richerme, P.; Lee, A.; Campbell, W.; Monroe, C. Coherent imaging spectroscopy of a quantum many-body spin system. *Science* **2014**, *345*, 430−433.
(63) Smith, J.; Lee, A.; Richerme, P.; Neyenhuis, B.; Hess, P. W.; Hauke, P.; Heyl, M.; Huse, D. A.; Monroe, C. Many-body localization in a quantum simulator with programmable random disorder. *Nat. Phys.* **2016**, *12*, 907.
(64) Zhang, J.; et al. Observation of a discrete time crystal. *Nature* **2017**, *543*, 217.
(65) Tran, M. C.; Guo, A. Y.; Baldwin, C. L.; Ehrenberg, A.; Gorshkov, A. V.; Lucas, A. The Lieb-Robinson Light Cone for Power-Law Interactions. 2021. arXiv:2103.15828, arXiv.org e-Print archive, https://arxiv.org/abs/2103.15828.
(66) Kim, K.; Chang, M.-S.; Korenblit, S.; Islam, R.; Edwards, E. E.; Freericks, J. K.; Lin, G.-D.; Duan, L.-M.; Monroe, C. Quantum simulation of frustrated Ising spins with trapped ions. *Nature* **2010**, *465*, 590−593.
(67) Feit, M.; Fleck, J. Solution of the Schrödinger equation by a spectral method II: Vibrational energy levels of triatomic molecules. *J. Chem. Phys.* **1983**, *78*, 301−308.
(68) Kouri, D. J.; Huang, Y.; Hoffman, D. K. Iterated Real-Time Path Integral Evaluation Using a Distributed Approximating Functional Propagator and Average-Case Complexity Integration. *Phys. Rev. Lett.* **1995**, *75*, 49−52.
(69) Hoffman, D. K.; Nayar, N.; Sharafeddin, O. A.; Kouri, D. Analytic banded approximation for the discretized free propagator. *J. Phys. Chem. A* **1991**, *95*, 8299−8305.
(70) Nielsen, M. A.; Chuang, I. L. *Quantum Computation and Quantum Information*; Cambridge University Press, Cambridge, 2000.
(71) Kunz. On the Equivalence Between One-Dimensional Discrete Walsh-Hadamard and Multidimensional Discrete Fourier Transforms. *IEEE Trans. Comput.* **1979**, *C-28*, 267−268.
(72) Lias, S. G.; Liebman, J. F.; Levin, R. D. Evaluated Gas Phase Basicities and Proton Affinities of Molecules; Heats of Formation of Protonated Molecules. *J. Phys. Chem. Ref. Data* **1984**, *13*, 695−808.
(73) Perrin, D. D. *Dissociation Constants of Organic Bases in Aqueous Solution: Supplement 1972*; Franklin Book Company, 1972; Vol. *1*.
(74) Perrin, C. L.; Nielson, J. B. 'Strong' Hydrogen Bonds in Chemistry and Biology. *Annu. Rev. Phys. Chem.* **1997**, *48*, No. 511.
(75) Gerlt, J. A.; Kreevoy, M. M.; Cleland, W. W.; Frey, P. A. Understanding Enzymic Catalysis: The Importance of Short, Strong Hydrogen Bonds. *Chem. Biol.* **1997**, *4*, 259.
(76) Warshel, A.; Papazyan, A.; Kollman, P. A. On Low-Barrier Hydrogen-Bonds and Enzyme Catalysis. *Science* **1995**, *269*, 102.
(77) Cleland, W. W.; Kreevoy, M. M. Low-Barrier Hydrogen-Bonds and Enzymatic Catalysis. *Science* **1994**, *264*, 1887.
(78) Yandulov, D. V.; Schrock, R. R. Reduction of Dinitrogen to Ammonia at a Well-Protected Reaction Site in a Molybdenum Triamidoamine Complex. *J. Am. Chem. Soc.* **2002**, *124*, 6252.
(79) Harris, D. F.; Lukoyanov, D. A.; Shaw, S.; Compton, P.; Tokmina-Lukaszewska, M.; Bothner, B.; Kelleher, N.; Dean, D. R.; Hoffman, B. M.; Seefeldt, L. C. The Mechanism of N_2 Reduction Catalyzed by Fe-Nitrogenase Involves Reductive Elimination of H_2. *Biochemistry* **2018**, *57*, 701−710.
(80) Perrin, C. L. Are Short, Low-Barrier Hydrogen Bonds Unusually Strong. *Acc. Chem. Res.* **2010**, *43*, 1550−1557.
(81) Pietrzak, M.; Wehling, J. P.; Kong, S.; Tolstoy, P. M.; Shenderovich, I. G.; Lopez, C.; Claramut, R. M.; Elguero, J.; Denisov, G. S.; Limbach, H.-J. Symmetrization of Cationic Hydrogen Bridges of Protonated Sponges Induced by Solvent and Counteranion Interactions as Revealed by NMR Spectroscopy. *Chem. - Eur. J.* **2010**, *16*, 1679−1690.
(82) Li, X.; Oomens, J.; Eyler, J. R.; Moore, D. T.; Iyengar, S. S. Isotope dependent, temperature regulated, energy repartitioning in a low-barrier, short-strong hydrogen bonded cluster. *J. Chem. Phys.* **2010**, *132*, No. 244301.
(83) Li, X.; Moore, D. T.; Iyengar, S. S. Insights from first principles molecular dynamics studies toward infrared multiple-photon and single-photon action spectroscopy: Case study of the proton-bound dimethyl ether dimer. *J. Chem. Phys.* **2008**, *128*, No. 184308.
(84) Korevaar, J. Pansions and the Theory of Fourier Transforms. *Trans. Am. Math. Soc.* **1959**, *91*, 53−101.
(85) Yu, S.; Zhao, S.; Wei, G. Local spectral time splitting method for first- and second-order partial differential equations. *J. Comput. Phys.* **2005**, *206*, 727−780.
(86) Abramowitz, M.; Stegun, I. A. *Handbook of Mathematical Functions with Formulas, Graphs, and Mathematical Tables*; US Government Printing Office, 1964; Vol. *55*.
(87) Hoffman, D. K.; Arnold, M.; Kouri, D. J. Properties of the optimum distributed approximating function class propagator for discretized and continuous wave packet propagations. *J. Phys. Chem. B* **1992**, *96*, 6539−6545.
(88) Iyengar, S. S.; Jakowski, J. Quantum wave packet ab initio molecular dynamics: An approach to study quantum dynamics in large systems. *J. Chem. Phys.* **2005**, *122*, No. 114105.

https://doi.org/10.1021/acs.jctc.1c00688
J. Chem. Theory Comput. 2021, 17, 6713−6732

(89) Grossmann, A.; Morlet, J. Decomposition of Hardy Functions into Square Integrable Wavelets of Constant Shape. *SIAM J. Math. Anal.* **1984**, *15*, 723−736.
(90) Strang, G. Wavelets and Dilation Equations: A Brief Introduction. *SIAM Rev.* **1989**, *31*, 614−627.
(91) Daubechies, I.; Heil, C. Ten Lectures on Wavelets. *Comput. Phys.* **1992**, *6*, 697.
(92) Strang, G.; Nguyen, T. Q. *Wavelets and filter banks*; SIAM, 1996.
(93) Billing, G. D. Quantum dressed classical mechanics. *J. Chem. Phys.* **2001**, *114*, 6641−6653.
(94) Ben-Nun, M.; Quenneville, J.; Martínez, T. J. Ab Initio Multiple Spawning: Photochemistry from First Principles Quantum Molecular Dynamics. *J. Phys. Chem. A* **2000**, *104*, 5161−5175.
(95) Heller, E. J. Time-dependent approach to semi-classical dynamics. *J. Chem. Phys.* **1975**, *62*, 1544−1555.

https://doi.org/10.1021/acs.jctc.1c00688
J. Chem. Theory Comput. 2021, 17, 6713−6732